A Westerbork blind HI imaging survey of the Perseus-Pisces filament in the Zone of Avoidance

Ramatsoku, Mpati Analicia

3

The WSRT PP ZoA II. The 3C 129 cluster

M. Ramatsoku[a,b,c], M.A.W Verheijen[a], R.C. Kraan-Korteweg[b],T.H. Jarrett[b], K. Said[b], A.C. Schröder[d]

[a] Kapteyn Astronomical Institute, University of Groningen, Landleven 12, 9747 AV Groningen, The Netherlands

[b] Department of Astronomy, University of Cape Town, Private Bag X3, Rondebosch 7701, South Africa

[c] ASTRON, Netherlands Institute for Radio Astronomy, Postbus 2, 7990 AA Dwingeloo, The Netherlands

[d] South African Astronomical Observatory (SAAO), PO Box 9, 7935 Observatory, Cape Town, South Africa

Submitted to Monthly Notices of the Royal Astronomical Society, 09 May 2017.

Abstract

We present a catalogue of 261 galaxy members of the 3C 129 cluster. The cluster, located at $z \approx 0.02$, forms part of the Perseus-Pisces filament and is obscured in the optical due to its location in the Zone of Avoidance. Galaxies are identified in the near-infrared using the J and K band data provided by the UKIDSS Galactic Plane Survey within an area of radius of 1.1° centred on the X-ray emission of the cluster at $\ell, b \approx 160.52°, 0.27°$. Of these galaxies 26 have known redshifts, of which 23 from our HI observations and 3 from optical spectroscopy. A comparison of the 3C 129 cluster K-band luminosity function with those of well-known galaxy clusters at similar redshifts shows that the galaxy density in the core of the 3C 129 cluster is similar to that of the Norma cluster and slightly less than in the Coma cluster. This places the 3C 129 cluster among the richest galaxy clusters in the Perseus-Pisces filament. From an assessment of the spatial and velocity distributions of the 3C 129 cluster galaxies with redshifts, we measured a velocity of $cz = 5227 \pm 171$ km s^{-1} and $\sigma = 1097 \pm 252$ km s^{-1} for the main cluster, with a substructure in the cluster outskirts at $cz = 6923 \pm 71$ km s^{-1} with $\sigma = 422 \pm 100$ km s^{-1}. The presence of this substructure is consistent with previous claims based on the X-ray analysis that the cluster is not yet virialised and may have undergone a recent merger.

Keywords: galaxy clusters; photometry; 3C 129 cluster; near-infrared

3.1 Introduction

At the nodes of large filamentary structures in the Universe, clusters of galaxies are continually growing and evolving as they accrete matter from the surrounding large-scale structures (Ouchi et al. 2005, Springel et al. 2005, Muldrew, Hatch & Cooke 2015). Galaxy clusters are the largest gravitationally bound systems (Borgani et al. 2001, Allen et al. 2004, Vikhlinin et al. 2009, Mantz et al. 2010) and critical cosmological probes. Much of our present understanding on galaxy formation and evolution has been based on observing galaxies in cluster environments (Bell et al. 2004, Miller et al. 2009). Nearby galaxy clusters have particularly shaped our understanding because we are able to study them at a level of detail that would not be possible for clusters at high redshifts (eg., Drinkwater, Gregg & Colless 2001, Chung et al. 2009, Hammer et al. 2010, Karachentsev et al. 2014, Weinzirl et al. 2014).

Our attention was drawn to the nearby 3C 129 cluster when it was uncovered as an overdensity in our Nançay survey of 2MASX galaxies in the Zone of Avoidance (van Driel et al. 2009, Ramatsoku et al. 2014). It is part of the expansive Perseus-Pisces Supercluster (PPS) at a redshift of $z \approx 0.02$. Very little is known about this cluster's galaxy population despite being part of this well-studied filament (Giovanelli & Haynes 1985a, Haynes & Giovanelli 1986, Haynes et al. 1988, Hudson et al. 1997, Hanski et al. 2001). This is due to its location at extremely low Galactic latitudes, $\ell, b \approx 160.52°, 0.27°$ (Ebeling, Mullis & Tully 2002), where severe extinction ($A_B \geq 5$ mag) and stellar confusion in the plane of the Milky Way (MW) make locating even major overdensities in the galaxy distribution inherently difficult and unreliable (Kraan-Korteweg & Lahav 2000b, Roman, Iwata & Saitō 2000).

This galaxy cluster was first identified with the Uhuru satellite (Forman et al. 1978) in the 2−6 keV band as the X-ray source 4U 0446+44. It was subsequently observed with the ROentgen SATellite (ROSAT)[1], the European Space Agency X-ray Observatory (EXOSAT)[2] and the Einstein[3] satellite. It is also detected and listed in the CIZA catalogue as CIZA J0450.0+4501 (Ebeling, Mullis & Tully 2002). From analyses of these data, Leahy & Yin (2000) reported an X-ray temperature of kT=5.5 keV, a total luminosity of 2.7×10^{44} erg s^{-1} in the $0.2 - 10$ keV and a total cluster mass of 4.7×10^{14}M$_\odot$. For comparison, the Coma cluster has an X-ray temperature of 8.0 keV, a total luminosity of 7.26×10^{44} erg s^{-1} (Ebeling et al. 1998b) and a total cluster mass of $13 \pm 2 \times 10^{14}$M$_\odot$ (Hughes 1989).

The cluster contains two radio galaxies, 3C 129 and 3C 129.1 ($cz = 6236$ and 6655 km s^{-1}, respectively (Spinrad 1975)) with jets extending far into the intra-cluster medium (ICM). 3C 129 is a well-studied (Owen et al. 1979, Jaegers & de Grijp 1983, Taylor et al. 2001, Harris, Krawczynski & Taylor 2002, Lal & Rao 2004, Murgia et al. 2016) head-tail radio source with a curved tail that extends over 427 kpc (Krawczynski et al. 2003) and a total flux density of ~ 5.3 Jy at 1400 MHz (White & Becker 1992), while 3C 129.1 is a wide-angle tail radio source with a total flux density of ~ 1.9 Jy at 1400 MHz (Condon et al. 1998).

[1] https://heasarc.gsfc.nasa.gov/docs/rosat/rosat3.html
[2] https://heasarc.gsfc.nasa.gov/docs/exosat/exosat.html
[3] https://heasarc.gsfc.nasa.gov/docs/einstein/heao2_about.html

Due to the high extinction layer of the Milky Way, most of what is known about the cluster is from its X-ray and radio source properties since most of its constituent galaxies had not been observed before. For this reason we decided to perform a census of the galaxy population of this cluster by conducting a deep, blind, HI imaging survey with the Westerbork Synthesis Radio Telescope[1] (WSRT). This was done using a mosaic of about $3^\circ \times 3^\circ$ covering the cluster and its immediate surrounding regions of the PPS (Ramatsoku et al. 2016).

Our aims are to investigate the large-scale and sub-structure associated with the 3C 129 galaxy cluster and to determine its relevance to flow fields around it and the larger PPS. As evident in the 2MASS survey of extended sources, this large scale structure envelops the cluster as it crosses from the southern to northern Galactic hemispheres (Jarrett 2004) (see also Fig. 3.1). Our data will also aid in efforts by the 2MASS Tully-Fisher survey (2MTF; Masters, Springob & Huchra 2008) since they complement the inner ZoA regions ($b \approx |5^\circ|$) that are excluded from optical spectroscopy. Moreover, since we covered a wide area of the cluster with our HI imaging survey, we will be able to characterise the various environments in and around the cluster to study the environmental effects on the population of galaxies therein.

HI is an ideal diagnostic tool for studying processes in clusters because of its sensitivity to the environment. It has also proved most effective at detecting galaxies at low Galactic latitudes (Kraan-Korteweg et al. 1994, van Driel et al. 2009, Henning et al. 2010, McIntyre et al. 2015). However, it is unsuitable for tracing the dominant galaxy population of clusters which primarily comprises gas-poor, early-type galaxies. On the other hand, these early-type galaxies stand out at near-infrared wavelengths, particularly in the J and K bands. Combining the HI and NIR data provide a versatile and robust tool for conducting an inventory of the galaxy population in clusters, particularly behind the Galactic Plane (GP) where dust extinction primarily presents a challenge for optical wavelengths.

[1] http://www.astron.nl/radio-observatory/

In this paper we explore the NIR colour-magnitude properties of galaxies within the WSRT HI mosaic to identify cluster members of the 3C 129 cluster and to complement our HI detections at NIR wavelengths. This is achieved using data from the UKIDSS Galactic Plane Survey (Lucas et al. 2008).

The layout of the paper is as follows: In Section 3.2 we give a summary of the HI sample and discuss the near-infrared photometry of the UKIDSS images. The colour-magnitude relation and cluster membership selection are discussed in Sec. 3.3. A subset of the catalogue of the cluster galaxies and images are described and presented in Sec. 3.3.2, with the full catalogue and images given in Appendix B. The near-infrared properties and luminosity function of the cluster are discussed in Sec. 3.3.2. We describe the structure of the cluster in Sec. 3.4.1 and discuss along with a summary of the main results in Sec. 3.5.

We assume a Λ cold dark matter cosmology with $\Omega_{\rm M} = 0.3, \Lambda_{\Omega} = 0.7$ and a Hubble constant $\rm H_0 = 70$ km s^{-1} Mpc^{-1} throughout this paper.

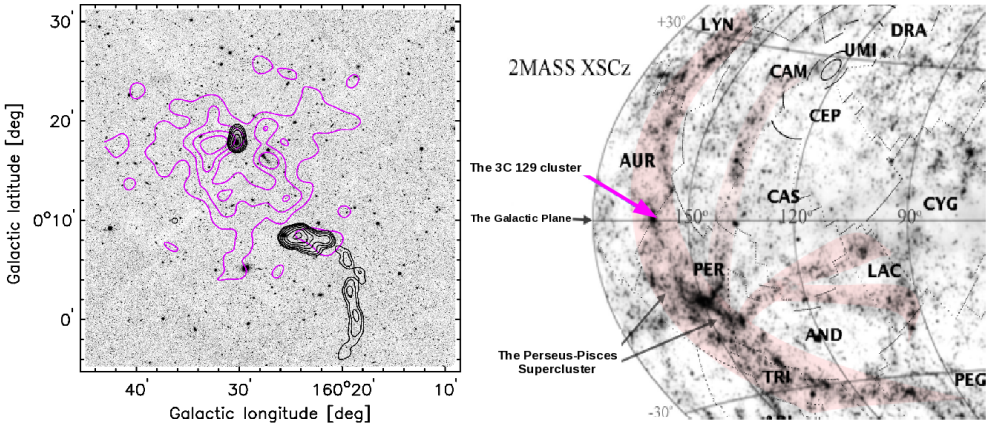

Figure 3.1 – Left panel: The central region of the 3C 129 cluster ($\sim 37' \times 37'$) showing the K-band UKIDSS image. The VLA 1424 MHz contours of the radio sources (NVSS; Condon et al. 1998) are overlaid in black. The 3C 129 is the head-tailed source with a curved tail on the right and the wide-angle tailed radio source on the left is 3C 129.1. The X-ray 0.1 - 2.4 keV emission from ROSAT is overlaid in magenta. Right panel: An Aitoff Galactic projection of the galaxy distribution extracted from the 2MASS Galaxy Catalog (XSCz) in the Local Universe shown from the northern hemisphere (Jarrett 2004). The image highlights the large filamentary structure of the PPS shaded in pink. The 3C 129 cluster lies in the GP crossing at $\ell \approx 161°$.

3.2 Data Samples

3.2.1 The HI data

We refer the reader to Ramatsoku et al. (2016) for a detailed description of the HI observations and data. Here, only a brief summary is provided:

The 21 cm HI-line imaging survey was conducted using the Westerbork Synthesis Radio Telescope (WSRT) comprising 35 pointings each with an integration time of 12 hours, in a hexagonal mosaic centred at $\ell, b \approx 160°, 0.5°$ which is where the Perseus-Pisces Supercluster crosses the Zone of Avoidance. The total sky area covered was $\sim$9.6 deg^2, with a survey rms sensitivity of 0.36 mJy/beam over the radial velocity range of $cz = 2400-16600$ km s^{-1}, with 16.5 km s^{-1} and $23'' \times 16''$ velocity and angular resolution respectively. A total of 214 HI galaxies in the HI mass range of $5 \times 10^7 - 2 \times 10^{10}$ M$_\odot$, with 80 galaxies spatially resolved, were detected over the entire radial velocity range. Of these galaxies, 87 were detected at a redshift of the 3C 129 cluster ($cz \sim 4000 - 8000$ km s^{-1}). The rest were found in the foreground and background of the cluster, at redshifts of, $cz = 2400-4000$ km s^{-1} and $cz \sim 10000-16600$ km s^{-1}, respectively. The footprint of our HI observations is shown in blue in Fig. 3.2.

3.2.2 The Near-Infrared Data

The cluster is prominent in the 2MASX catalogue as illustrated in the right panel of Fig. 3.1. However, we extracted our near-infrared sample of galaxies from images provided by the UKIRT Infrared Deep Sky Survey (UKIDSS: Lawrence et al. 2007) because of its improved depth and spatial resolution. We used Data Release 10 (DR10) of a sub-survey of UKIDSS, the Galactic Plane Survey (GPS), which covers an area of 1800 deg^2 to a 5σ $K(2.2\mu m)$-band depth of 18.8 mag (Vega)(Lucas et al. 2008).

The UKIDSS-GPS with a pixel scale of $0.2''$/pix (after microstepping) and an average seeing of $0.8''$ is highly successful at separating stars from galaxies further from the Galactic mid-plane ($|b| \gtrsim 5°$). However, it suffers from confusion at lower Galactic latitudes. At these regions visual inspection is still a superior method for identifying galaxies (Lucas et al. 2008). For this reason, prior to visual inspection, we opted to use the SExtractor software (SEXTRACTOR version 2.8.6; Bertin & Arnouts 1996) to extract sources from sixteen overlapping UKIDSS-GPS images of size $1° \times 1°$, supplemented by smaller images ($\sim 30' \times 30'$) which together cover the entire HI mosaic survey footprint of the WSRT (see Fig. 3.2).

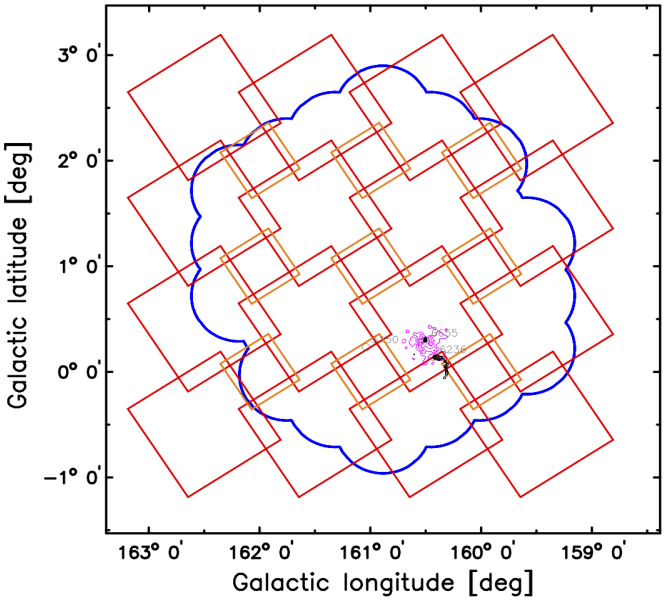

Figure 3.2 – The projected sky distribution of the observed WSRT hexagonal mosaic in blue. Coverage of the near-infrared tiles from the UKIDSS - GPS data is outlined in red. The X-ray emission is shown in magenta and the position of the contours of the radio sources 3C 129 and 3C 129.1 are shown in black.

For the purposes of source detection, the K-band was used. It is less affected by Galactic dust extinction and provides higher signal-to-noise ratios compared to the $J(1.2\mu m)$- or $H(1.6\mu m)$-bands.

The source detection performed by SEXTRACTOR uses an algorithm that registers a detection when a set number of pixels are connected as specified by the detection parameters, DETECT_MINAREA and DETECT_THRESH. An empirically two-fold approach was adopted to set these parameter values; for sources with pixel values above 9σ, a minimum of 10 adjacent pixels was required. Sources between $3\sigma - 9\sigma$ were only accepted, if they had a minimum of 50 adjacent pixels.

After identifying the sources, an analysis was conducted to deblend objects that are identified as connected on the sky based on the deblending parameters, DEBLEND_MINCONT and DEBLEND_NTHRESH which were chosen to be 0.001 and 32 respectively. These empirical values were selected after performing tests with a wide range of values and verifying results by visual inspection to ensure that spurious detections were minimised and no obvious sources were missed. We estimated the GLOBAL background noise with a small mesh set by, BACK_SIZE = 64. This size

was chosen to prevent an overestimation of the background due to wings of very bright sources. The set of SEXTRACTOR parameters adopted for detecting sources in the UKIDSS-GPS K-band images is given in Table. 3.1.

Table 3.1 – Parameters for SEXTRACTOR 2.8.6.

Parameter	Value
DETECT_MINAREA	50 (10 for sources above 9σ)
DETECT_THRESH	3 (9 for min. of 50 adjacent pixels)
ANALYSIS_THRESH	3
FILTER	Y
FILTER_NAME	default.conv
DEBLEND_NTHRESH	32
DEBLEND_MINCONT	0.001
CLEAN	Y
CLEAN_PARAM	1.0
MASK_TYPE	CORRECT
PHOT_APERTURES	5
PHOT_AUTOPARAMS	2.5, 3.5
PHOT_PETROPARAMS	2.0, 3.5
SATUR_LEVEL	422784/ADU
MAG_ZEROPOINT	24.105
GAIN	4.5/e-/ADU
GAIN_KEY	GAIN
PIXEL_SCALE	0.4/arcsec
SEEING_FWHM	0.8/arcsec
STARNNW_NAME	default.nnw
BACK_SIZE	64
BACK_FILTERSIZE	3
BACKPHOTO_TYPE	GLOBAL

3.2.3 Star-Galaxy Separation

SEXTRACTOR parameters described in section 3.2.2, were optimised to limit the number of stars and spurious detections. The optimal combination of threshold and minimum area was selected, relying on sources that appeared to be galaxies based on their visual inspection. However, the high stellar density in the GP resulted in many point-source detections (stars). In this section we present a step-by-step description of how the star-galaxy classification was performed.

(a) SEXTRACTOR stellarity index

A preliminary star-galaxy classification was conducted based on SEXTRACTOR's stellarity index (CLASS_STAR) which is a dimensionless parameter that characterises objects as point-like or extended. This classification parameter, CLASS_STAR, is based on the neural-network analysis approach that compares the point spread function to the object scale and then provides a confidence level estimate of the classification which ranges from 0 for galaxies to 1 for stars. Figure 3.3 shows the distribution of the CLASS_STAR values of $\sim$ 460,000 detected objects. Two clear populations with CLASS_STAR values of 0 and 1 are evident. The histogram for sources classified as galaxies decreases sharply for CLASS_STAR = 0.0 to 0.35, it then flattens and rises steeply from CLASS_STAR = 0.8 to 1.0. Based on the CLASS_STAR values, objects were initially classified in the following manner:

CLASS_STAR $\leq$ 0.35 (Galaxies),

0.35 $<$CLASS_STAR $<$ 0.8 (Stars or galaxies),

CLASS_STAR $\geq$ 0.8 (Stars),

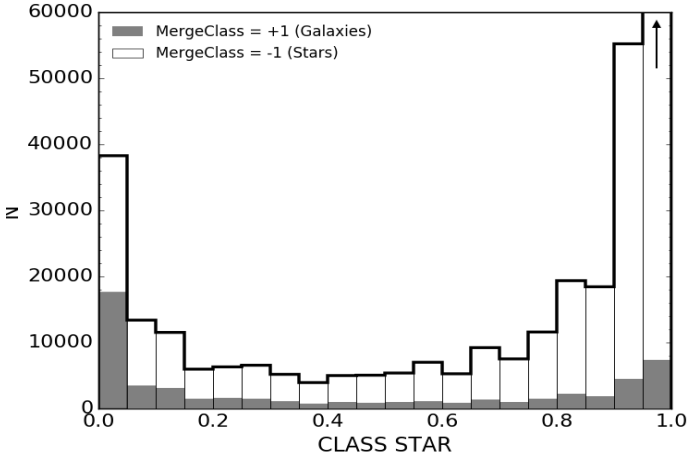

Figure 3.3 – The distribution of SEXTRACTOR stellarity index, CLASS_STAR of all objects found in the UKIDSS-GPS searched images. All objects with CLASS_STAR $>$ 0.8 are stars, those with CLASS_STAR $<$ 0.35, galaxies and 0.35 $<$CLASS_STAR $<$ 0.8 are ambiguous objects. The open histogram shows the distribution of objected labeled as stars in the UKIDSS catalogue (MERGECLASS=-1) and the filled histogram are those labelled as galaxies (MERGECLASS=+1). The horizontal arrow points to a higher number count of $\sim 10^5$ in that bin that is not shown in the plot.

(b) UKIDSS-GPS star-galaxy separator

To increase the reliability of objects classified as galaxies by CLASS_STAR, their classifications were cross-correlated with the UKIDSS-GPS catalogue which also provides a star-galaxy separation parameter, MERGEDCLASS. This parameter is based on quantitative measurements in the J, H and K passbands of the observed radial profiles by the UKIDSS data reduction pipeline (Dye et al. 2006). The profiles are characterised by the "mergeClassStat" parameter and identified as either point-like, resolved or an artifact. Resolved sources are assigned large "mergeClassStat" values and smaller values are associated with point-like sources. Additionally, the UKIDSS-GPS further separates galaxies from stars by making cuts based on the difference between the Petrosian (resolved) magnitude and the point source magnitude (Lucas et al. 2008). Galaxies are assigned parameter value of MERGECLASS$=+1$ and stars are assigned MERGECLASS$=-1$.

(c) Visual inspection

We found that the CLASS_STAR and MERGECLASS parameters are not reliable in all circumstances. For instance, out of all sources with CLASS_STAR $= 0.0$ only about 47% were classified as galaxies by MERGECLASS (see Fig. 3.3). As a result we needed to ensure that galaxies were not missed by only depending on the star galaxy classification based on these parameters, particularly in the ambiguous $0.35 <$ CLASS_STAR < 0.8 range. This necessitated a further step to improve the reliability of the classification of each object and to remove any spurious detections. For this task we conducted a visual inspection of all objects with CLASS_STAR < 0.8. Objects with CLASS_STAR > 0.8 were not inspected visually since only 0.05% of the objects in these bins had MERGECLASS $= +1$. This was performed using DS9 by inspecting the J, H and K bands three-colour (RGB) composite images. The extended nature of galaxies made them readily distinguishable in this manner.

After removing duplicate detections in overlapping regions of the UKIDSS images, artifacts and stars, the final sample consisted of 9737 unique galaxies over the full WSRT mosaic.

3.2.4 Star-Subtraction

The high stellar density affects images of galaxies at low Galactic latitudes. It is therefore important to take additional steps to remove stars superimposed on the galaxies to acquire accurate photometry. This was done by fitting a point spread function (PSF) to stars and subsequently removing them from the galaxy. For this purpose we used a four-step script based on the IRAF routine KILLALL (Buta & McCall 1999), which in turn is based on DAOPHOT tasks (Stetson 1987). The four steps were as follows: (a) We used IMSTAT to determine the rms and sky background in the image; (b) We modelled the galaxy using ELLIPSE and BMODEL, and removed this model from the image. It should however, be noted that galaxy structures such as spiral arms may be not be modelled fully and might result in residuals in the galaxy-subtracted image; (c) We used SEXTRACTOR to detect bright stars that are above 3.5σ in the image in which the galaxy has been subtracted. The PSF photometry of these sources was then determined using DAOPHOT (tasks ALLSTAR and PHOT) and removed from the image. This step was repeated for fainter stars above 1.8σ. To mitigate against misidentifying residual structures as stars, we required these stars to be detected by DAOFIND at the 2σ threshold; (d) The two lists with the bright and faint stars were combined and removed from the original image using the SUBSTAR task; (e) The residuals resulting from imperfect PSF fits to stars in the image were found and removed. We repeated steps (b) to (e) four times, each time improving the galaxy model, which resulted in a more reliable star removal.

Figure 3.4 shows example images for three galaxies in our sample before (left panel) and after (right panel) star-subtraction. It illustrates that this star removal procedure performs reasonably well. In fact, it has been shown by Woudt et al. (2005) and Mutabazi et al. (2014), through simulations of subtracting artificial stars added to non-crowded fields, that removing stars this way has a minimal effect (less than 0.01 mag on average) on the galaxy photometry.

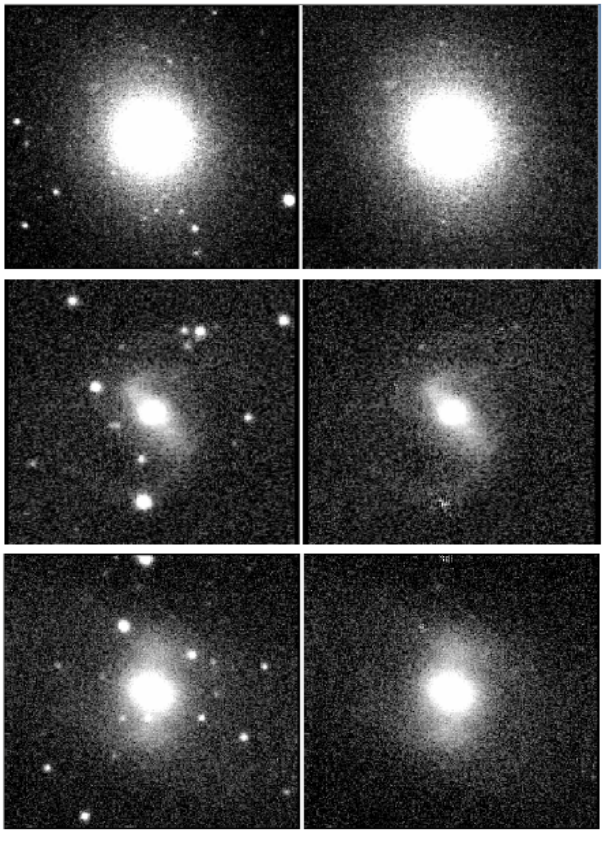

Figure 3.4 – Postage stamp examples of K-band images of galaxies before (left panels) and after star-subtraction (right panels).

3.2.5 The NIR Photometry

After subtracting all the stars we extracted the galaxy photometric parameters. Since UKIDSS photometric parameters are only measured within circular apertures which are inadequate for elongated galaxies, we used customised python scripts developed by K. Said[1] and W. Williams[2] based on a combination of SEXTRACTOR and IRAF tasks.

Astrometry of positions: First, the central positions of galaxies were determined by adding the three images from the J+H+K bands and measuring the intensity-weighted centroid. This method of determining positions is more accurate as it measures the centre of the galaxy from higher signal-to-noise images (Jarrett et al. 2000).

[1] khaled@ast.uct.ac.za
[2] w.williams5@herts.ac.uk

Ellipticities and geometries: Next, ellipticities and position angles were determined individually from the J, H and K band images. The IRAF task ELLIPSE was used to fit ellipses to the galaxy image. Ellipticities, $\epsilon = (1 - b/a)$ and position angles (ϕ; counter clockwise from North) were then fitted at semi-major axis intervals, while keeping the central coordinates, X and Y fixed. The ELLIPSE task produced tables containing the intensity (in counts) within the ellipse and the ellipticity and position angle at each semi-major axis interval including their errors. Then the galaxy's position angle and ellipticity were determined to be the average value in the outer disk between 1σ - 2σ isophotes, where σ is the sky background rms.

Magnitudes: Finally, the isophotal magnitudes were measured within elliptical apertures in all bands (J, H, K). The K-band surface brightness $\mu = 20$ mag arcsec^{-2} isophote was adopted to determine the isophotal radius ($r_{k_{20}}$). Fiducial magnitudes were measured within this same aperture of radius $r_{k_{20}}$ for the J, H, K-bands. All the magnitudes are based on the Vega calibration.

3.2.6 Photometric checks

To check our photometric consistency, we derived from the UKIDSS images galaxy magnitudes within a $7''$ radius circular aperture and compared these with their counterparts in the 2MASX catalogue (Jarrett et al. 2000) in the same $7''$ circular aperture. Sources in both catalogues were matched if they were separated by less than $1.5''$. We used this small correlation radius of $1.5''$ because the UKIDSS WFCAM astrometric calibration was derived from 2MASS (Hodgkin et al. 2009), which has a positional accuracy of about $0.5''$. Only galaxies with reliable photometry (as flagged in the 2MASX catalogue) were compared. We found 363 counterparts in the 2MASX catalogue.

In Fig. 3.5, we show a comparison of our UKIDSS photometry with that of the 2MASX. The comparison relation used is:

$$\Delta m = m_{2MASX} - m_{UKIDSS}. \tag{3.1}$$

By this equation, a positive Δm indicates that 2MASX magnitudes are fainter than our UKIDSS magnitudes. The offsets given in the top right corners of Fig. 3.5 indicate that the 2MASX galaxies are slightly brighter than their UKIDSS counterparts. These offsets can be attributed to the

higher resolution of the UKIDSS images with a seeing of $\sim 0.8''$ compared to 2MASS with a seeing of $\sim 3.0''$. The improved resolution of the UKIDSS allows for the detection and subtraction of fainter foregrounds stars that would otherwise contribute to the galaxy's brightness within the measurement aperture. It is also probable that the different filters used could have contributed to these slight offsets. The UKIDSS uses the Mauna Kea Observatory (MKO; Hodgkin et al. 2009) filter set which is slightly different from the 2MASS filter set (Cohen, Wheaton & Megeath 2003).

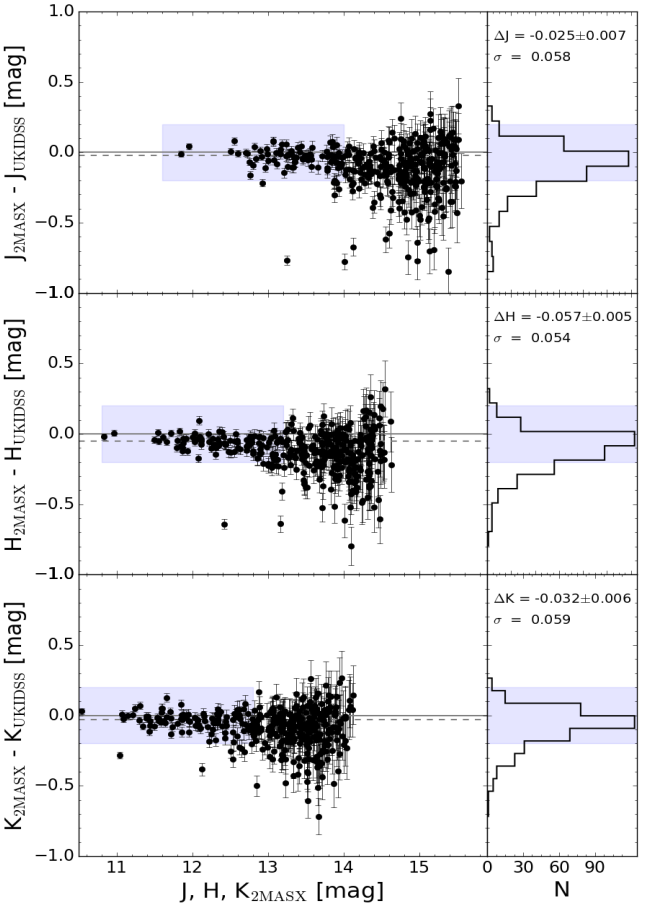

Figure 3.5 – Comparison between the 2MASX and UKIDSS circular aperture magnitudes measured within a $7''$ radius for the J (top), H (middle) and K (bottom) bands. The median offset between the two surveys is indicated by the dashed line and is printed in the top right legend. This median was determined within areas marked by the blue shades also marked in the histograms.

3.2.7 Extinction

Galaxies in the ZoA tend to have their brightness reduced due to the dust obscuration in the Milky Way. This effect is less prominent in the near-infrared compared to the optical, but it is nonetheless not negligible. Within our WSRT field the Galactic extinction values range from $A_K = 0.16 - 0.56$ mag (see Fig. 7 of Ramatsoku et al. 2016).

We correct for this effect using the extinction law;

$$\frac{A_\lambda}{E(B-V)} = R_\mathrm{v}, \tag{3.2}$$

where A_λ is the extinction in a given band and $E(B-V)$ is the colour reddening from Schlegel, Finkbeiner & Davis (1998) with the Schlafly & Finkbeiner (2011) correction factor of 0.86 applied. The value for $\mathrm{R_V} = 3.1$ is given by Schlegel, Finkbeiner & Davis (1998). Using the parametrisation by Fitzpatrick (1999) we derive the extinction in the J, H and K bands;

$$A_J = 0.741E(B-V), \tag{3.3}$$

$$A_H = 0.456E(B-V), \tag{3.4}$$

$$A_K = 0.310E(B-V). \tag{3.5}$$

The effect of extinction on our galaxies is low given that our field has a median extinction of $A_K = 0.29 \pm 0.05$ mag, however this is not negligible. This extinction also translates into a reduction of the isophotal radius of the galaxy due to the loss of the fainter, low surface brightness outer regions.

3.3 The Colour-Magnitude Relation

The colour-magnitude relation (CMR) has been shown to be a powerful technique for selecting galaxies in clusters since they form a distinct linear feature in the colour-magnitude diagram (Visvanathan & Sandage 1977). This feature, known as the red sequence, has a well-defined slope that evolves with redshift and a small (< 0.1 mag) intrinsic scatter (Bower, Lucey & Ellis 1992, Gladders et al. 1998, López-Cruz, Barkhouse & Yee 2004, Stott et al. 2009). In addition to the tight CMR, galaxies in regular clusters have a radial distribution that is typically centrally concentrated

(Dressler 1980). They also form the dominant population at the bright end of the galaxy luminosity function and create a high contrast against the background, thus making them easily recognisable in surveys (Gladders et al. 1998).

To find galaxy member candidates of the 3C 129 cluster, we use the CMR in the near-infrared to identify the red sequence feature as well as the angular on-sky projection distribution to detect clustering. The advantage of using this technique is that it is not affected by projection effects since any random distribution of galaxies will not form a coherent red sequence signature in the colour-magnitude diagram.

In Fig. 3.6 we present the NIR colour-magnitude diagram (CMD) of all 9737 galaxies within the observed WSRT mosaic (see Fig. 3.2). Colours were measured inside the $\mu_k = 20$ mag arcsec^{-2} fiducial isophotal aperture defined in the K-band and corrected for foreground extinction based on the DIRBE/IRAS maps as described in Sect. 3.2.7.

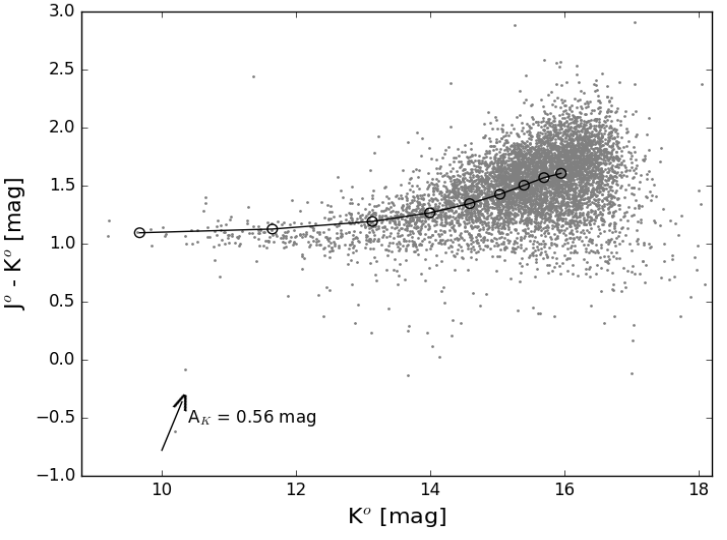

Figure 3.6 – The colour-magnitude diagram of 9737 sources from the UKIDSS-GPS within the WSRT mosaic (see Sect. 3.2.2). The reddening curve computed from redshift $z = 0.02$ to $z = 0.4$ is shown by black line with open circles representing the redshift bin and Galactic dust reddening vector for a K-band extinction of 0.56 mag is indicated with the arrow.

Two well-defined populations are apparent in this plot. The dominant population ($K^o < 12$ mag, $J^o - K^o \gtrsim 1.3$ mag) consists of redshifted background galaxies. The overlaid reddening curve[1] (Chilingarian, Melchior & Zolotukhin 2010) supports this claim. The other identifiable population is a slightly slanted band of galaxies that stretches between $8 \lesssim K \lesssim 16$ mag with colours, $J^o - K^o \approx 1.1$ mag. This second feature contains within it the red sequence of the 3C 129 cluster. Below the red sequence is a small population of blue outliers which were visually inspected and found to be close binary stars and/or artefacts that were missed during the star-galaxy separation process in the UKIDSS images (see Sect. 3.2.3).

3.3.1 The Red Sequence and Cluster Membership

To determine the galaxy cluster membership we used a three step process as follows:

Firstly, a region of the CMD containing the red sequence was selected and an estimate of the initial fit was made by visual inspection. All points deviating by more than 3σ from this initial fit were removed from the full sample. We then performed an iterative linear fit of the form, $J - K = \alpha K + c$ where the slope of the red sequence is denoted by α to points that were within $\pm 3\sigma$ of the initial fit. The final fit gives $(J - K)^o = -(0.023 \pm 0.002)K^o + 1.25$ with a 1σ dispersion of 0.039 mag. The slope matches that of the Coma cluster of $\alpha = -0.017 \pm 0.009$ (measured by Stott et al. 2009), which is at a similar redshift of $z \approx 0.02$ as the 3C 129 cluster. The $J - K$ colours of the red sequences are also comparable to that of galaxy clusters in the WIde-field Nearby Galaxy-cluster Survey (WINGS: Valentinuzzi et al. 2011). Galaxies within $\pm 3\sigma$ of the final fit formed the initial list of the cluster member candidates.

Secondly, we limited the relative background contamination in the initial sample list of red sequence galaxies by only selecting galaxies with $r_{k_{20}} > 3''$. This was motivated by the fact that the red sequence of the cluster becomes less well-defined for galaxies with $r_{k_{20}} < 3''$ which typically corresponds to magnitudes of $K^o \gtrsim 15.5$ mag; these are likely dwarf galaxies which are of no interest to this study.

[1] http://kcor.sai.msu.ru

Thirdly, we defined a radius r_{cl} of the cluster centred on the ROSAT X-ray emission. This cluster radius was chosen based on the spatial distribution (cf. Fig. 3.12) of the red sequence galaxies which have radii larger than $r_{k_{20}} > 3''$ out to where they became sparsely distributed. Assuming a redshift of $z = 0.02$ the radius was found to be $r_{cl} \approx 1.7$ Mpc ($\sim 0.8 r_A$[1]). It corresponds to about $1.34 R_{200}$, where R_{200} is the radius at which the average interior density of the cluster is $200 \times \rho_c$, where ρ_c is the critical density of the Universe. The R_{200} of the 3C 129 cluster is ~ 1.24 Mpc based on the $0.1 - 2.4$ keV band measurements by ROSAT (Piffaretti et al. 2011). We then only selected red sequence galaxies within $r_{cl} < 1.34 R_{200}$ as cluster members.

After applying the steps outlined above, we obtained a sample of 250 galaxy members of the 3C 129 cluster which lie on the red-sequence. Of these galaxies 13 were already previously detected in HI (Ramatsoku et al. 2016). The CMD of all galaxies on the red sequence is shown in Fig 3.7. In addition, we included 11 more galaxies with $r_{k_{20}} < 3''$ that were detected in HI within the velocity window and the defined radius of the cluster on the sky regardless of their location on the red-sequence. Thus the final sample of the 3C 129 cluster members comprises 261 galaxies.

We note that we cannot measure the contamination of the final sample by background galaxies without redshift measurements. However, it has been previously shown that this method of finding galaxy clusters members in both the infrared and optical wavelengths results in a background contamination of less than 5% (Gladders & Yee 2000).

3.3.2 Morphologies of the Cluster Members

Figure 3.8 shows the CMD of the cluster with galaxies separated into approximate morphologies based on a visual inspection and a subjective estimate of their bulge-to-disk ratios, their ellipticities and compactness. The morphological classification was independently conducted and adjudicated by co-authors. This classification is only meant to distinguish large-scale trends and to give a general description of galaxy morphologies in the cluster. Galaxies were classified into five broad groups of early-types (E/S0), early spirals (eS) such as Sa/Sb, medium spirals (mS) which were typically of Sc/Sd type, the late-type spirals (ℓS) which were

[1] r_A is the Abell radius

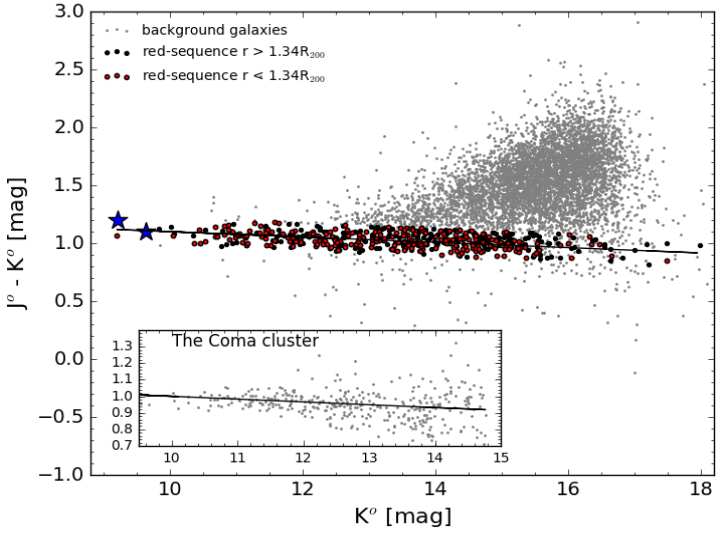

Figure 3.7 – The colour-magnitude diagram showing the red sequence signature of the 3C 129 cluster in red with the two blue stars identifying the bright radio sources, 3C 129 and 3C 129.1. The fitted slope, $\alpha = -0.023 \pm 0.002$ mag of the cluster is illustrated by the black solid line and compared to that of the Coma cluster using 2MASX data in the inserted CMD. Black points are galaxies outside the cluster radius of $r_{cl} < 1.34R_{200}$ and grey points are mostly background galaxies.

mostly Sdm, and Irregular (Irr) galaxies without any discernible structure. In Fig. 3.8 we also indicate with black squares, the galaxies detected in HI (with UKIDSS counterparts) within the velocity range and radius of the cluster.

Figure 3.8 shows early-type galaxies (E/S0) and the early-spirals to be mostly located on the bright end of the red sequence. This is to be expected given that we are evaluating a potentially rich cluster which tends to have more of these bright early-type galaxies than star forming late-type galaxies.

The mid-range spiral galaxies (mS) show no obvious trends in the CMD except that they are predominantly at magnitudes fainter than most of the early-type galaxies. There is a number of these type of galaxies ($\sim$ 23%) detected near the centre of the cluster (see also Figs. 3.12 and 3.13 in Sect. 3.4). Interestingly, they were not detected in HI, suggesting they might be stripped of their gas by ram-pressure from the ICM upon infall, thus resulting in HI deficiencies. Judging by their morphologies alone, these should have otherwise been detected in our HI observations.

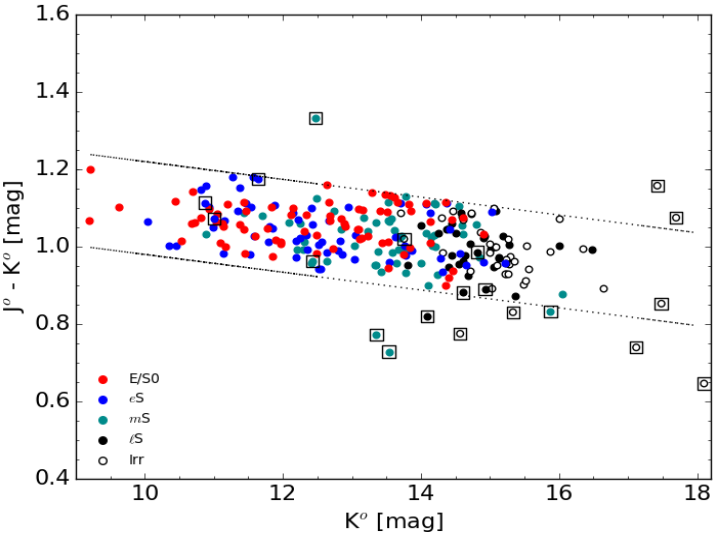

Figure 3.8 – The CMD of the 3C 129 cluster with members shown in red in Fig. 3.7 separated by morphologies defined in the colours in the legend. Circles are the red-sequence galaxies and those enclosed in squares are HI detected galaxies within the radius of the cluster and velocity range. The dotted lines show the $\pm 3\sigma$ rms dispersion (0.12 mag) from the fitted red sequence relation: $J - K = -0.023K + 1.25$. Magnitudes and colours are measured inside the K-band 20 mag arcsec^{-2} isophotal fiducial aperture and are corrected for Galactic extinction.

Late-type spirals and Irregular galaxies are mostly found at the fainter end of the CMD at $K^o \gtrsim 14$ mag. These are typically LSB galaxies which could have lost their gas through tidal stripping or interaction with the ICM (Conselice, Gallagher & Wyse 2003). On the other hand, most of the HI detected galaxies also populate this end of the CMD, but tend to be slightly bluer ($J^o - K^o \lesssim 1.0$) than their LSB counterparts. They are located in the cluster outskirts where we expect less interaction and where we expect galaxies to have retained their gas.

Analyses of these populations of galaxies as well as the effect of the various environments in which they reside, requires a more comprehensive analysis than presented in this paper. Here we only present a cursory description and we will study and discuss the detailed nature of these galaxies in a forthcoming paper.

The catalogue of cluster galaxies

A full catalogue of the 261 cluster members is presented in Appendix B, Table B. Galaxies are listed in ascending order of their K-band magnitudes (from the brightest to the faintest). For each galaxy a $1.2' \times 1.2'$ image in the J, H and K band was extracted. The false colour (RGB) postage stamps of these images are shown in Figure B in the same order as the catalogue. Galaxy morphologies are printed at the bottom of the images. The 24 galaxies that were detected in HI are framed in cyan. The first 30 entries of the catalogue and their corresponding images are shown in Table. 3.2 and Fig 3.9, respectively.

The columns are as follows:

Column 1 - The galaxy identifying number.

Column 2- Unique identifiers based on the Right Ascension (RA) and Declination (Dec) ZoAJhhmmss.ss±ddmmss.s.

Columns 3 & 4 - Equatorial coordinates, RA and Dec (J2000), respectively in degrees.

Columns 5 & 6 - Galactic longitude and latitude in degrees.

Column 7 - Ellipticity in the K-band at the 20 mag arcsec^{-2} isophote.

Column 8 - The K-band position angle in degrees, measured from celestial North to East.

Column 9 - The K_{20} isophotal major-axis radius in arcseconds.

Columns 10 & 11 & 12 - J, H and K band fiducial isophotal magnitudes (not corrected for foreground extinction).

Column 13 - The line of sight Galactic reddening in magnitudes.

Column 14 - $J - K$ colours, corrected for foreground extinction.

Column 15 - The estimated morphology of galaxies.

Column 16 - The radial velocities from the WSRT HI measurements plus optical velocities for the two galaxies 3C 129 and 3C 129.1.

Table 3.2 – Near−infrared parameters of the first 30 entries of 3C 129 cluster galaxies. The full catalogue is available in Appendix B

ID no.	Unique ID	RA	Dec	ℓ	b	ϵ_K	ϕ_K	r_{K20}	J_{K20}	H_{K20}	K_{20}	$E(B\text{-}V)$	J^o-K^o	Type	v_{rad}
	ZoA	deg	deg	deg	deg		deg	$''$	mag	mag	mag	mag	mag		km s^{-1}
(1)	(2)	(3)	(4)	(5)	(6)	(7)	(8)	(9)	(10)	(11)	(12)	(13)	(14)	(15)	(16)
1	J044908.26+445540.3	72.284	44.928	160.490	0.086	0.17	24.71	28.10	10.96 ± 0.02	9.94 ± 0.02	9.51 ± 0.02	0.89	1.07	E/S0	—
2	J045006.67+450305.8	72.528	45.052	160.505	0.298	0.20	65.00	37.30	11.21 ± 0.04	10.10 ± 0.04	9.59 ± 0.04	0.98	1.20	E/S0	6655*
3	J044909.06+450039.4	72.288	45.011	160.427	0.142	0.10	−60.00	25.60	11.50 ± 0.03	10.46 ± 0.04	10.00 ± 0.04	0.94	1.10	E/S0	6236$^{\times}$
4	J045145.56+443602.6	72.940	44.601	161.039	0.235	0.40	60.00	22.80	11.75 ± 0.03	10.82 ± 0.03	10.35 ± 0.04	0.79	1.07	*e*S	5086^{+}
5	J044939.78+440922.1	72.416	44.156	161.141	−0.337	0.09	−55.01	12.79	12.05 ± 0.02	11.16 ± 0.02	10.76 ± 0.02	0.65	1.01	E/S0	—
6	J044842.39+454818.5	72.177	45.805	159.769	0.593	0.40	−61.15	21.62	12.25 ± 0.02	11.23 ± 0.02	10.77 ± 0.02	1.12	1.00	*e*S	—
7	J045245.69+450106.2	73.190	45.018	160.829	0.638	0.44	85.11	19.63	12.31 ± 0.02	11.23 ± 0.02	10.78 ± 0.02	0.94	1.12	E/S0	—
8	J045219.88+451546.1	73.083	45.263	160.592	0.734	0.50	−60.00	25.90	12.23 ± 0.05	11.26 ± 0.05	10.83 ± 0.06	0.91	1.00	*e*S	—
9	J045326.75+441900.7	73.361	44.317	161.449	0.288	0.06	26.77	14.31	12.32 ± 0.02	11.38 ± 0.02	10.96 ± 0.02	0.69	1.06	E/S0	—
10	J045045.92+450659.7	72.691	45.117	160.529	0.428	0.27	0.36	13.39	12.62 ± 0.02	11.56 ± 0.02	11.05 ± 0.02	1.00	1.14	E/S0	—
11	J044719.31+441701.6	71.830	44.284	160.774	−0.576	0.47	−73.54	16.96	12.50 ± 0.02	11.56 ± 0.02	11.06 ± 0.02	0.69	1.15	*e*S	4993
12	J044843.25+445216.0	72.180	44.871	160.486	−0.007	0.11	32.33	9.98	12.54 ± 0.02	11.54 ± 0.02	11.11 ± 0.02	0.84	1.07	E/S0	—
13	J044459.45+453344.1	71.248	45.562	159.534	−0.059	0.30	−23.53	14.62	12.83 ± 0.02	11.73 ± 0.02	11.19 ± 0.02	1.35	1.06	E/S0	—
14	J044429.89+442914.8	71.125	44.487	160.291	−0.827	0.31	44.80	14.65	12.81 ± 0.02	11.78 ± 0.02	11.23 ± 0.02	0.98	1.16	*e*S	—
15	J044724.21+445928.3	71.851	44.991	160.244	−0.107	0.80	−35.00	31.50	12.64 ± 0.05	11.67 ± 0.05	11.25 ± 0.07	0.84	1.03	*m*S	—
16	J045414.90+450315.1	73.562	45.054	160.967	0.864	0.17	−41.28	19.00	12.79 ± 0.02	11.75 ± 0.02	11.29 ± 0.02	0.93	1.10	*e*S	6269
17	J045129.31+451852.0	72.872	45.314	160.458	0.652	0.57	−35.96	17.04	12.86 ± 0.02	11.84 ± 0.02	11.31 ± 0.02	1.04	1.10	E/S0	—
18	J045028.01+443407.6	72.617	44.569	160.916	0.037	0.70	−74.56	15.98	12.74 ± 0.02	11.79 ± 0.02	11.32 ± 0.02	0.80	1.07	E/S0	—
19	J045156.57+445815.0	72.986	44.971	160.774	0.496	0.47	−12.60	14.73	12.79 ± 0.02	11.79 ± 0.02	11.33 ± 0.02	0.94	1.05	*e*S	—
20	J045251.94+444122.5	73.216	44.690	161.095	0.443	0.56	63.37	16.94	12.90 ± 0.02	11.92 ± 0.02	11.47 ± 0.02	0.85	1.07	*e*S	—
21	J045018.46+454152.2	72.577	45.698	160.031	0.738	0.27	24.97	12.06	13.08 ± 0.02	11.99 ± 0.02	11.49 ± 0.02	1.17	1.08	E/S0	—
22	J045324.45+451127.6	73.352	45.191	160.768	0.835	0.40	29.03	12.08	12.97 ± 0.02	11.93 ± 0.02	11.50 ± 0.02	0.98	1.05	E/S0	—
23	J044753.50+443250.9	71.973	44.547	160.638	−0.328	0.10	25.00	13.10	12.88 ± 0.04	11.87 ± 0.05	11.52 ± 0.06	0.84	1.00	E/S0	—
24	J044734.77+452912.6	71.895	45.487	159.885	0.237	0.41	50.35	8.87	13.14 ± 0.02	12.05 ± 0.02	11.56 ± 0.02	1.19	1.06	E/S0	—
25	J045332.55+453232.6	73.386	45.542	160.510	1.076	0.39	−23.08	14.16	13.09 ± 0.02	12.03 ± 0.02	11.56 ± 0.02	0.98	1.11	E/S0	—
26	J044639.43+454052.2	71.664	45.681	159.633	0.240	0.41	85.72	12.30	13.12 ± 0.02	12.08 ± 0.02	11.57 ± 0.02	1.25	1.01	E/S0	—
27	J044730.43+454548.7	71.877	45.764	159.666	0.406	0.20	47.01	10.49	13.14 ± 0.02	12.11 ± 0.02	11.62 ± 0.02	1.25	0.98	*e*S	—

Table 3.2 – Continued

ID no.	Unique ID	RA	Dec	ℓ	b	ϵ_K	ϕ_K	r_{K20}	J_{K20}	H_{K20}	K_{K20}	$E(B\text{-}V)$	J^o-K^o	Type	v_{rad}
	ZoA	deg	deg	deg	deg		deg	$''$	mag	mag	mag	mag	mag		km s^{-1}
(1)	(2)	(3)	(4)	(5)	(6)	(7)	(8)	(9)	(10)	(11)	(12)	(13)	(14)	(15)	(16)
28	J044953.41+451613.5	72.473	45.270	160.312	0.408	0.60	−60.00	15.10	13.33 ± 0.05	12.16 ± 0.04	11.71 ± 0.06	1.01	1.18	*e*S	—
29	J045032.79+445411.7	72.637	44.903	160.668	0.262	0.29	−10.36	12.04	13.26 ± 0.02	12.21 ± 0.02	11.71 ± 0.02	0.92	1.15	*e*S	—
30	J044940.04+451119.0	72.417	45.189	160.350	0.325	0.62	−10.81	13.76	13.23 ± 0.02	12.22 ± 0.02	11.72 ± 0.02	0.98	1.09	*e*S	—

[*] v_{opt}: Spinrad 1975
[×] v_{opt}: Spinrad 1975
[+] v_{opt} = 5150 (Takata et al. 1994)

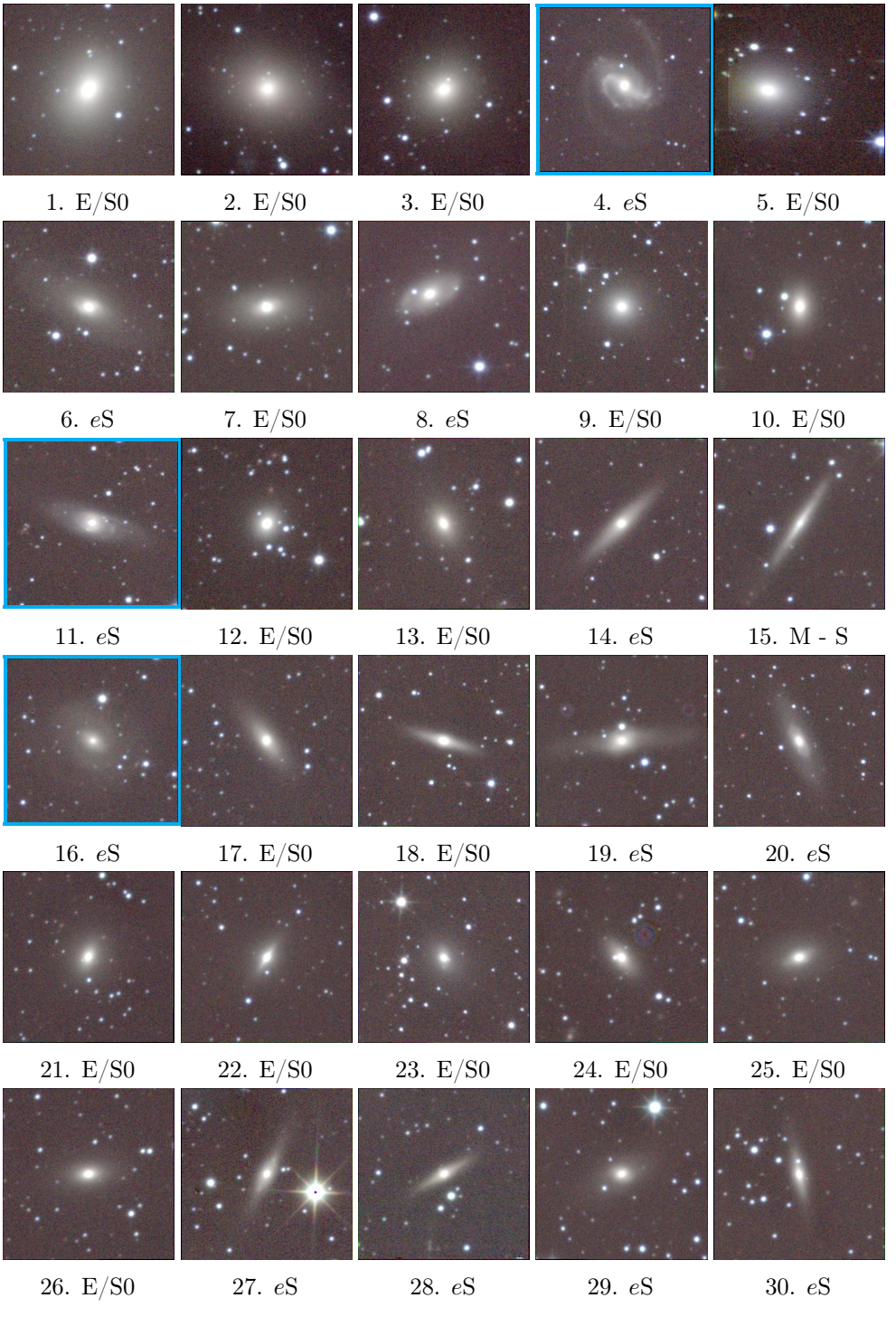

Figure 3.9 – The false-colour – J (blue), H (green) and K (red) representation ($1.2' \times 1.2'$) of the 30 brightest galaxies in the 3C 129 cluster. The cyan frames indicate HI detection in the WSRT HI-survey.

The 3C 129 cluster luminosity function

In this subsection we will assess the richness of the 3C 129 cluster based on the galaxy population identified in the UKIDSS-GPS images. We consider the 144 identified galaxies within the R_{500} radius of the cluster in order to make a fair comparison with the K-band luminosity functions (LF) of the well-studied, rich Coma and Norma galaxy clusters located at similar distances as the 3C 129 cluster. R_{500} is the radius at which the average interior density of the cluster is $500 \times \rho_c$, where ρ_c is the critical density of the Universe. For the 3C 129 cluster, $R_{500} = 0.87$ Mpc based on the ROSAT X-ray measurements in the $0.1 - 2.4$ keV bands (Piffaretti et al. 2011). We recall, however, that we lack spectroscopic redshifts for all but two of the early-type galaxies in the core of the 3C 129 cluster. Hence we cannot be certain that all galaxies we identify as cluster members are actually located in the cluster core.

We consider the fiducial, elliptical K-band aperture magnitudes, corrected for Galactic extinction. Figure 3.10 shows the distribution of these extinction corrected K^o-band magnitudes with a solid histogram while the dashed line shows the distribution of the non-corrected magnitudes. Based on our visual inspection of the UKIDSS-GPS images, we are confident that we have identified all galaxies brighter than $K \approx 15$ mag, corresponding to $K^o \approx 14.5$ mag. We refer to Table B and Fig. B for a visual impression of galaxies with these magnitudes.

The black symbols in Figure 3.11 show the inferred K^o-band LF of the 3C 129 cluster based on the number counts in 0.5 magnitude wide bins, normalised by the cluster's area within R_{500} (Mobasher et al. 2003). The error bars are derived from Poisson statistics while the open symbols indicate magnitude bins in which the number counts are estimated to be significantly affected by incompleteness. Given the severity and unknown small-scale patchiness of the Galactic extinction, we note that it is non-trivial to perform robust and quantitative completeness corrections. Therefore, we only consider the solid symbols in Figure 3.11 for our subsequent analysis.

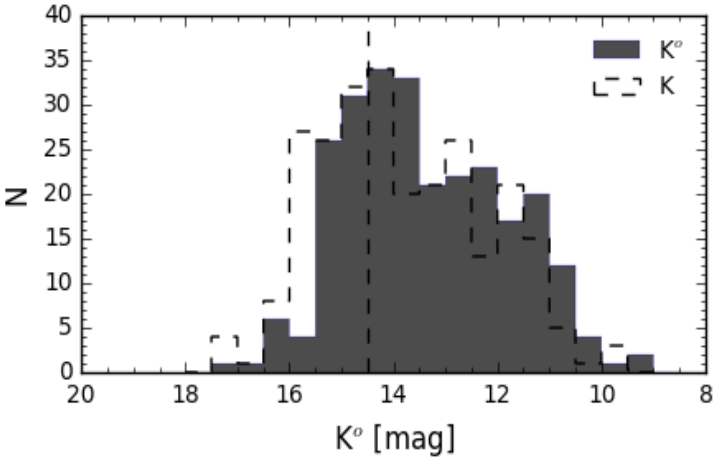

Figure 3.10 – Distribution of the fiducial isophotal magnitudes for the K-band. Histograms are plotted in 0.5 mag bins. The dashed histogram represents the observed magnitudes and the solid histogram the extinction-corrected magnitudes. The estimated completeness limit is shown by the vertical dashed line.

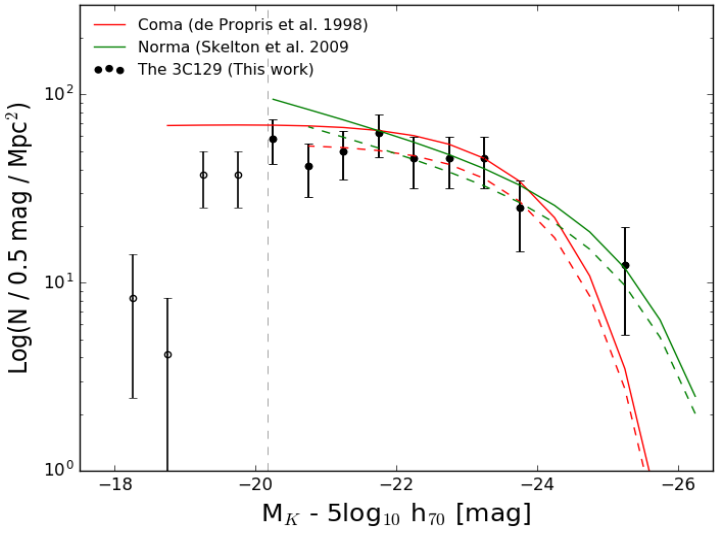

Figure 3.11 – Comparison of the K-band luminosity function per 0.5 mag bin of the 3C 129 cluster with two well known clusters at similar distances, the Norma (green) and Coma (red) clusters. The black points indicate the LF of the 3C 129 cluster out to an estimated completeness of $M_K \approx -20.2$ mag and open symbols are bins within which we expect to be incomplete. The dashed lines are the LF of the Coma (red) and Norma (green) clusters, normalised to the 3C 129 cluster.

The red solid line in Fig. 3.11 shows the K-band LF of the Coma cluster ($M_K^* = -24.0$ mag, $\alpha = -0.98$, $\phi^* = 76.0 \pm 3.0$ h$_{70}^2$ Mpc^{-2}) as derived by De Propris et al. (1998) while the green solid line indicates the K-band LF of the Norma cluster ($M_K^* = -25.4 \pm 0.8$ mag, $\alpha = -1.26 \pm 0.10$, $\phi^* = 27.8 \pm 2.4$ h$_{70}^2$ Mpc^{-2}) as derived by Skelton, Woudt & Kraan-Korteweg (2009). Note that the LF parameters of these two clusters are significantly different. We also refer to the result by De Propris (2017) who determined the average K-band LF for a sample of 24 galaxy clusters and found $M_K^* = -24.81 \pm 0.14$ mag and $\alpha = -1.41 \pm 0.10$, consistent with Skelton's result for the Norma cluster, while ϕ^* is not defined for this composite LF.

Here, we consider ϕ^* within R_{500} as a measure of a cluster's richness and a proxy for it's mass. We take the LF parameters for the Coma and Norma clusters, adopt and fix the corresponding values of M_K^* and α, and determine the value of ϕ^* by fitting these LFs to the solid black points in Fig.3.11. These fits are indicated by the dashed lines. This exercise resulted in values of $\phi^* = 59.4 \pm 6.3$ h$_{70}^2$ Mpc^{-2} for the Coma cluster and $\phi^* = 22.5 \pm 3.1$ h$_{70}^2$ Mpc^{-2} for the Norma cluster. This indicates that the galaxy density in the core of the 3C 129 cluster is similar to the central galaxy density in the Norma cluster and slightly less than in the Coma cluster. This finding is supported by the relative X-ray luminosities of the three clusters.

We did not conduct a detailed completeness analysis for the 3C 129 and are hampered by the lack of redshifts for the gas-poor galaxies. As a result no attempt was made to determine or fit a luminosity-function of the 3C 129 cluster.

Table 3.3 – A summary of parameters of comparison galaxy clusters.

Cluster	Distance	Lx$_{500}$	R$_{500}$	N	$M_{\rm Kcompl.}$
	Mpc	10^{44} erg s^{-1}	Mpc		mag
(1)	(2)	(3)	(4)	(5)	(6)
3C 129	89.1	0.9	0.87	144	-20.2 [1]
Norma	70.0	1.1	0.90	389	-19.5 [2]
Coma	98.9	3.4	1.14	649	-18.5 [3][1]

[1] This work
[2] Skelton, Woudt & Kraan-Korteweg 2009
[3] Eisenhardt et al. 2007

[1] This is an estimate, authors only list the H-band completeness limit

3.4 The Spatial Distribution of the 3C 129 Cluster Galaxies

The spatial distribution of all galaxies on our defined red-sequence is shown in Fig. 3.12. Members of the 3C 129 cluster are enclosed within the large dashed circle of radius of 1.7 Mpc centred on its X-ray emission ($\ell, b \approx 160.52°, 0.27°$). The smaller dotted circle encloses a prominent substructure to be discussed in Sect. 3.4.1. In this section we only discuss galaxies within the defined extent of the cluster (dashed circle).

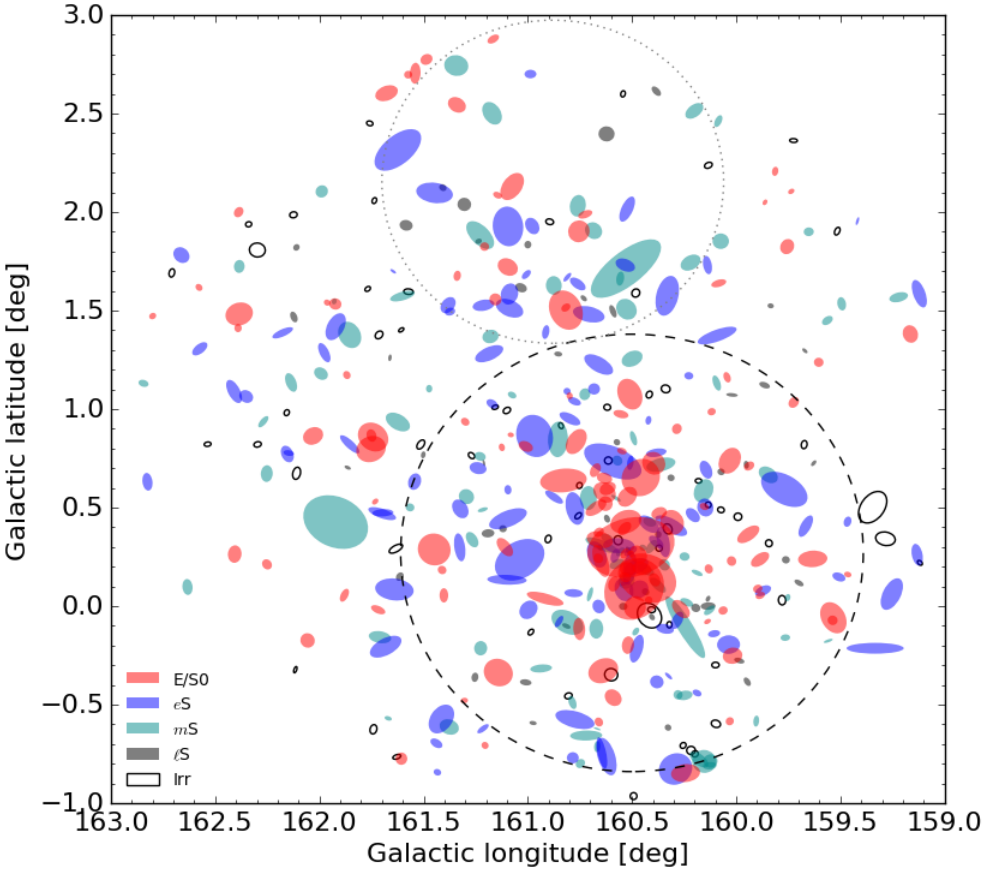

Figure 3.12 – The spatial distribution of galaxies on the red sequence. Points are shown relative to their radii, ellipticities and positions angles. The defined projected radius of the cluster, $r_{cl} = 1.7$ Mpc is shown by the black dashed line. The substructure of the cluster as described in Sect. 3.4.1 is denoted by the smaller dotted grey circle. The different colours illustrate the morphologies of the galaxies.

Galaxies within the inner region of the cluster of $r_{core} = 0.8$ Mpc, corresponding to its R_{500} (Piffaretti et al. 2011), are highly concentrated in the centre and are mostly early-type galaxies (E/S0). At larger projected radii the number of spirals (eS to Irr) increases steadily while the number of E/S0 galaxies decreases.

The spatial distribution in Fig. 3.12 is essentially a demonstration of the classical morphology-density relation (Dressler 1980). Most studies of the morphology-density (T - Σ) or morphology-radius (T - R) relation in galaxy clusters often use a composite of a large number of clusters to obtain an adequately high number of galaxies for each morphological type (Dressler 1980, Goto et al. 2003, Thomas & Katgert 2006). However, these composite (T - Σ) or (T - R) relations often lose information on the individual clusters. They also introduce large uncertainties given the large and sometimes inhomogeneous samples of clusters at different redshifts that are combined to make one cluster (Andreon 1996, van Dokkum et al. 2000).

To study the (T - R) relation specific to the 3C 129 cluster, we use a sample of all our classified galaxies (N=261). We show the results in Fig. 3.13 where the azimuthally averaged fractions of the morphological types are plotted as function of the projected distance from the core of the cluster to the outskirts. The fraction of E/S0 galaxies decreases from ∼36% in the core to almost 22% in the outskirts of the cluster. The early spirals (eS) fraction increases from 24% and peaks to 29% where the E/S0 population is lowest at $r_{cl} = 1.1$ Mpc and then decreases rapidly to 22% similar to the E/S0 fraction. On the other hand, ℓS and Irr galaxies show the opposite trend with an increasing fraction from the core towards the cluster outskirts. The morphology-radius relation of the 3C 129 cluster shows an obvious morphological segregation that is qualitatively consistent with those of the centrally concentrated rich clusters (Dressler et al. 1997).

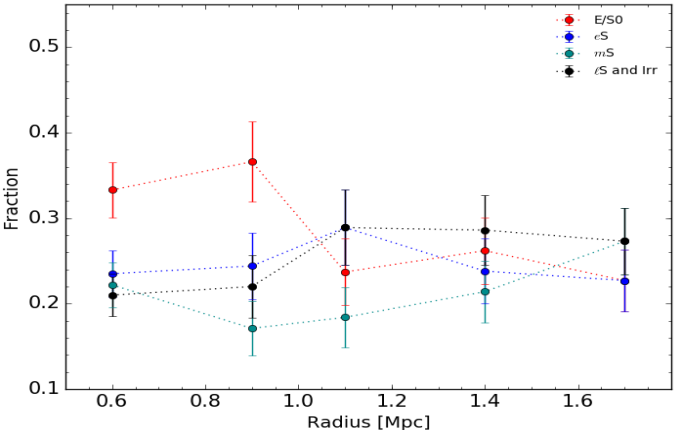

Figure 3.13 – The morphology-radius relation for the E/S0 (red), eS (blue), mS (darkcyan), ℓS & Irr (black) members of the cluster.

3.4.1 Substructure in the 3C 129 Cluster

Projected density distribution

To investigate the possible presence of substructure we analyse the projected galaxy number densities. Although this method ignores the redshift information it is optimal at identifying substructures with enhanced densities that are relatively large in separation (Pinkney et al. 1996). For the galaxies on the red sequence we study the projected galaxy number density using the bivariate kernel density estimator (Feigelson & Babu 2012),

$$f_{kern}(\mathbf{x},\mathbf{h}) = \frac{1}{n\prod_{j=1}^{p} h_j} \sum_{i=1}^{n} \left[\prod_{j=1}^{p} h_j Gk\left(\frac{\mathbf{x}_i - \mathbf{X}_{ij}}{h_{ij}}\right)\right] \tag{3.6}$$

where $p = 2$ is the number of variables, which are Galactic coordinates (ℓ, b) in our case represented by $\mathbf{X}_i = \mathbf{X}_{i1}, \mathbf{X}_{i2}$, with the smoothing length (bandwidth), $\mathbf{h} = (h_1, h_2)$. The number of galaxies is denoted by n and the bivariate Gaussian kernel function by Gk.

The resulting density map constructed with the red sequence galaxies is plotted in Fig. 3.14. It shows a distribution that is slightly elongated North-East to South-West in Galactic coordinates. This is possibly related to an intrinsically more elongated mass distribution of the large-scale filamentary structure (PPS) within which this cluster is embedded. Upon closer inspection two distinct structures become apparent. A dom-

inant density peak corresponds to the 3C 129 cluster centre, located at $(\ell, b) \approx (160.52°, 0.27°)$. The other, a more diffuse density peak about 2.9 Mpc (assuming $z = 0.02$) north from the cluster core located near $(\ell, b) \approx (160.88°, 2.20°)$, indicates a substructure, henceforth called the 3C129-A group.

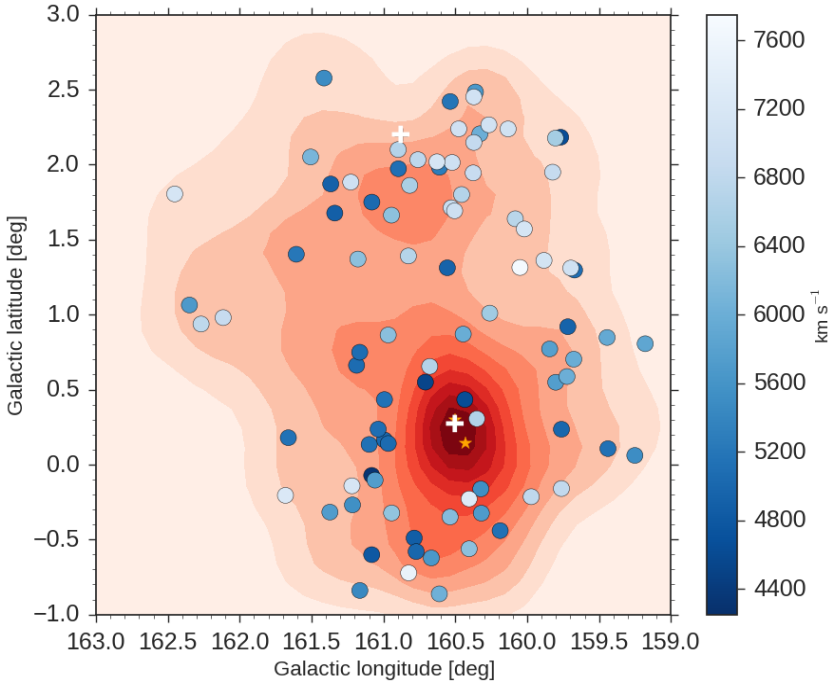

Figure 3.14 – The 2-dimensional kernel density map of galaxies on the red-sequence (red) in position space. Dots in gradient blues are galaxies detected in HI over the radial velocity range of the 3C 129 cluster (4000 - 8000 km s^{-1}). The displayed colour bar is the velocity range of the HI galaxies. The two white plus markers indicate the position of the X-ray emission over which the cluster is centred and the location near which the 3C129-A group lies.

A comparison with the X-ray emission map in Fig. 3.1 reveals that the core of the cluster is closely aligned with the X-ray gas emission. The X-ray contours are irregular and are not associated with any X-ray point source in the cluster. Thus supporting what was inferred by Leahy & Yin (2000) that 3C 129 cluster is under assembly through a merger and it is possibly growing along the filament.

Furthermore, we compared this galaxy projected density distribution with the spatial distribution of galaxies detected in H I in the velocity range of the cluster, marked by gradient blue dots. The latter shows the 3C129-A group to be more populated by H I-rich galaxies and also shows galaxies to have distinctly higher velocities than those around the core of the 3C 129 cluster. Furthermore, a relatively smaller number of H I detections was found in the core of the cluster, thus indicative of a gas removal mechanism taking place in this region. The implication of this is beyond the scope of this paper and will be discussed in detail in a paper that follows where we will be analysing the environmental effects on the H I properties of the galaxies.

Velocity Distribution

Having established the existence of the projected 3C129-A substructure in association with the 3C 129 cluster, we now investigate the radial velocity distribution of their constituent galaxies. We do this by using the 87 galaxies with measured H I radial velocities within the velocity range of the cluster's parent supercluster (PPS) of 4000 - 8000 km s^{-1} with and without a NIR-counterpart (Ramatsoku et al. 2016). A visual inspection of Fig. 3.14 indicates a bimodal velocity distribution of the H I detections. To check whether the velocity distribution is indeed statistically different from a Gaussian distribution we applied a Lilliefors test (see Feigelson & Babu 2012). The resulting p-value is $p < 0.01$ which indicates that the null hypothesis, which states that the full distribution is Gaussian, can be rejected, thus consistent with the presence of substructure in the radial velocity distribution.

We estimate the mean radial velocities of the two structures by selecting 43 H I-detected galaxies within a radius of 1.1° centred on the cluster's centre, and 44 within a radius of 0.8° centred on the 3C129-A group (see Fig. 3.12). The latter's radius was chosen to be as large as possible while maintaining mutual exclusivity with the 3C 129 cluster. The velocity distributions of the galaxies selected in the two structures are shown in Fig. 3.15. We fit two Gaussian profiles and obtained $cz = 5227 \pm 171$ km $s^{-1}$and $\sigma = 1097 \pm 252$ km s^{-1} for the 3C 129 cluster and $cz = 6923 \pm 71$ km s^{-1} and $\sigma = 422 \pm 100$ km s^{-1} for the 3C129-A group. We note that the velocity dispersion of the cluster is higher than that which was determined from the β-model of the cluster of $\sigma = 765$ km s^{-1} (Leahy & Yin 2000) but also note that our measurement is subject to large

uncertainties given the lack of optical spectroscopy for gas-poor galaxies in the cluster core.

Combining the results from the velocity and density distribution analysis we find a distinct substructure to the north of the 3C 129 cluster with higher velocity and more gas-rich spirals. Although the line-of-sight velocity difference of $cz_{gr} - cz_{cl} = 1696 \pm 185$ km s^{-1} is quite large, it is possible that the 3C129-A group is falling into the cluster. However, our sample is not large enough for a robust dynamical analysis to confirm this. A more detailed analysis can only be conducted with more redshifts of the gas-poor galaxies in the cluster and the immediate surrounding regions.

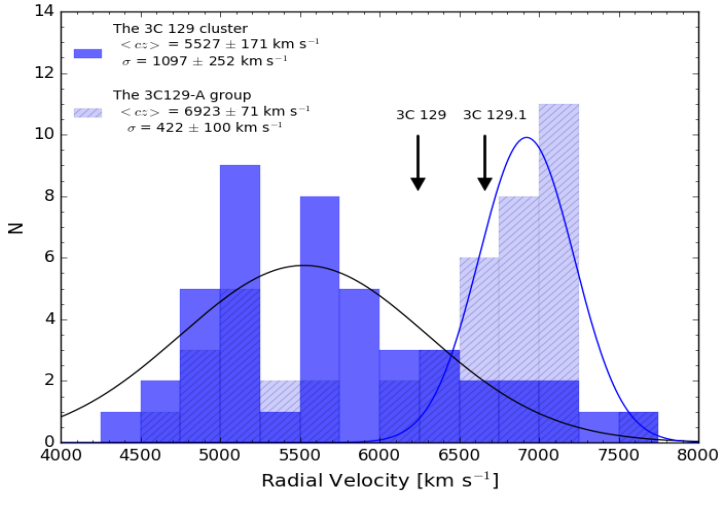

Figure 3.15 – The distribution of radial velocities of the 3C 129 cluster (dark blue) and its northern substructure; 3C 129-A (hatched light blue). Velocities bins are 250 km s^{-1} wide. The black line is a fitted Gaussian profile of the 3C 129 cluster and blue line for the 3C 129-A group. The radial velocities of the radio sources, 3C 129 and 3C 129.1 are indicated by arrows.

3.5 Summary and Discussions

We combined near-infrared images and colours from the UKIDSS Galactic Plane Survey with HI data from the Westerbork Synthesis Radio Telescope, in and around the 3C 129 cluster to identify its galaxy members. This was done by analysing the properties of the $J-K$ versus K magnitude of galaxies to define and fit the red-sequence of this cluster. The slope of its red sequence was found to be $\alpha = -0.023 \pm 0.002$ mag, similar to the Coma cluster ($\alpha = -0.017 \pm 0.009$). We determined the extent of the cluster, centred on the X-ray emission, out to a radius of 1.7 Mpc ($1.34R_{200}$). We obtained a sample of 261 identified 3C 129 cluster galaxies with $r_{k_{20}} > 3''$. Of these, 26 have redshift measurements, 23 from our WSRT HI observations and 3 from previous optical observations. A catalogue and colour images of the galaxy cluster members is presented.

The galaxies within the radius of 3C 129 cluster (1.7 Mpc) were used to present the cluster's luminosity function in the K-band. We compared this luminosity function with those of two well-known clusters at a similar redshift of $z \approx 0.02$, namely the Coma and Norma clusters. Results show that the galaxy density at the core of the 3C 129 cluster is comparable to that of the Norma cluster and slightly less than in the Coma cluster. This would place the 3C 129 cluster among the richest clusters in the Perseus-Pisces filament.

Using the high resolution ($0.8''$ seeing) UKIDSS images, we determined the broad morphologies of all the 261 cluster galaxies. We used the former to derive the morphology-radius relation of the cluster. A clear morphological segregation occurs at 0.6 - 0.9 Mpc from the cluster core, where the fraction of early-type galaxies increases inwards to more than 35%, while the fraction of late-type galaxies drops to about 16%. The segregation continues toward the cluster outskirts where the fraction of early-type galaxies drops to 22% and the fraction of late-types increases to almost 30%. A forthcoming study will assess how the environment may have affected the morphologies of these galaxies.

The spatial distribution of the galaxies in the 3C 129 cluster core shows a slight asymmetry and are aligned with the irregular X-ray emission that is not associated with any X-ray point source or any galaxy in the cluster. All these observations suggests that the system is non-Xray dominant (nXD) (Jones & Forman 1984). So the 3C 129 cluster could be

classified as an irregular nXD galaxy cluster. These features strengthen claims by Leahy & Yin (2000) that the cluster has undergone (or is undergoing) a merger and has not yet reached a dynamically relaxed state. This is supported by the identification of a substructure to the North of the main central region with a radial velocity distribution of $cz = 6923 \pm 71$ km s^{-1} and $\sigma = 422 \pm 100$ km s^{-1}, while the H I-detected galaxies around cluster core were measured to have, $cz = 5227 \pm 171$ km s^{-1} with $\sigma = 1097 \pm 252$ km s^{-1}. We suspect this substructure is infalling, which suggests the cluster is still growing by accreting from its parent large-scale structure that forms the Perseus-Pisces filament, which will have implications on the flow-fields around it and the larger PPS. However, this remains unconfirmed as more galaxy redshifts of the non H I-detected galaxies are required to conduct a detailed dynamical analysis of this cluster.

Acknowledgments

MR acknowledges financial support from the Ubbo Emmius Fund of the University of Groningen and the financial support provided by SKA South-Africa and the South African National Research Foundation. The SA and NL authors of this collaboration all benefitted tremendously from collaborative exchanges support by the NRF/NWO bilateral agreement for Astronomy and Astronomy Enabling Technologies. We would also like to thank W. Williams for the photometric contributions to the project. This research has also made use of the UKIRT Infrared Deep Sky Survey database. We acknowledge the UKIDSS support team, including M. Reads, S Hodgkin and P. Lucas for their various support on assessing the UKIDSS images. This work is part of MV's Vici research programme "The Panoramic Perspective on Gas and Galaxy Evolution" with project number 016.130.338, which is (partly) financed by the Netherlands Organisation for Scientific Research (NWO).

Appendix

3

Appendix B: The NIR Catalogue and Images

The near-infrared catalogue has the following columns:

Column 1 - The galaxy identifying number.

Column 2- Unique identifiers based on the Right Ascension (RA) and Declination (Dec) ZoAJhhmmss.ss±ddmmss.s.

Columns 3 & 4 - Equatorial coordinates, RA and Dec (J2000), respectively in degrees.

Columns 5 & 6 - Galactic longitude and latitude in degrees.

Column 7 - Ellipticity in the K-band at the 20 mag arcsec^{-2} isophote.

Column 8 - The K-band position angle in degrees, measured from celestial North to East.

Column 9 - The K_{20} isophotal major-axis radius in arcseconds.

Columns 10 & 11 & 12 - J, H and K band fiducial isophotal magnitudes (not corrected for foreground extinction).

Column 13 - The line of sight Galactic reddening in magnitudes.

Column 14 - $J - K$ colours, corrected for foreground extinction.

Column 15 - The estimated morphology of galaxies.

Column 16 - The radial velocities from the WSRT HI measurements plus optical velocities for the two galaxies 3C 129 and 3C 129.1.

Table B. Near−infrared parameters of the 3C 129 cluster galaxies.

ID no.	Unique ID	RA	Dec	ℓ	b	ϵ_K	ϕ_K	r_{K20}	J_{K20}	H_{K20}	K_{20}	$E(B\text{-}V)$	$J^o - K^o$	Type	v_{rad}
	ZoA	deg	deg	deg	deg		deg	$''$	mag	mag	mag	mag	mag		km s^{-1}
(1)	(2)	(3)	(4)	(5)	(6)	(7)	(8)	(9)	(10)	(11)	(12)	(13)	(14)	(15)	(16)
1	J044908.26+445540.3	72.284	44.928	160.490	0.086	0.17	24.71	28.10	10.96 ± 0.02	9.94 ± 0.02	9.51 ± 0.02	0.89	1.07	E/S0	—
2	J045006.67+450305.8	72.528	45.052	160.505	0.298	0.20	65.00	37.30	11.21 ± 0.04	10.10 ± 0.04	9.59 ± 0.04	0.98	1.20	E/S0	6655*
3	J044909.06+450039.4	72.288	45.011	160.427	0.142	0.10	−60.00	25.60	11.50 ± 0.03	10.46 ± 0.04	10.00 ± 0.04	0.94	1.10	E/S0	6236×
4	J045145.56+443602.6	72.940	44.601	161.039	0.235	0.40	60.00	22.80	11.75 ± 0.03	10.82 ± 0.03	10.35 ± 0.04	0.79	1.07	*e*S	5086+
5	J044939.78+440922.1	72.416	44.156	161.141	−0.337	0.09	−55.01	12.79	12.05 ± 0.02	11.16 ± 0.02	10.76 ± 0.02	0.65	1.01	E/S0	—
6	J044842.39+454818.5	72.177	45.805	159.769	0.593	0.40	−61.15	21.62	12.25 ± 0.02	11.23 ± 0.02	10.77 ± 0.02	1.12	1.00	*e*S	—
7	J045245.69+450106.2	73.190	45.018	160.829	0.638	0.44	85.11	19.63	12.31 ± 0.02	11.23 ± 0.02	10.78 ± 0.02	0.94	1.12	E/S0	—
8	J045219.88+451546.1	73.083	45.263	160.592	0.734	0.50	−60.00	25.90	12.23 ± 0.05	11.26 ± 0.05	10.83 ± 0.06	0.91	1.00	*e*S	—
9	J045326.75+441900.7	73.361	44.317	161.449	0.288	0.06	26.77	14.31	12.32 ± 0.02	11.38 ± 0.02	10.96 ± 0.02	0.69	1.06	E/S0	—
10	J045045.92+450659.7	72.691	45.117	160.529	0.428	0.27	0.36	13.39	12.62 ± 0.02	11.56 ± 0.02	11.05 ± 0.02	1.00	1.14	E/S0	—
11	J044719.31+441701.6	71.830	44.284	160.774	−0.576	0.47	−73.54	16.96	12.50 ± 0.02	11.56 ± 0.02	11.06 ± 0.02	0.69	1.15	*e*S	4993
12	J044843.25+445216.0	72.180	44.871	160.486	−0.007	0.11	32.33	9.98	12.54 ± 0.02	11.54 ± 0.02	11.11 ± 0.02	0.84	1.07	E/S0	—
13	J044459.45+453344.1	71.248	45.562	159.534	−0.059	0.30	−23.53	14.62	12.83 ± 0.02	11.73 ± 0.02	11.19 ± 0.02	1.35	1.06	E/S0	—
14	J044429.89+442914.8	71.125	44.487	160.291	−0.827	0.31	44.80	14.65	12.81 ± 0.02	11.78 ± 0.02	11.23 ± 0.02	0.98	1.16	*e*S	—
15	J044724.21+445928.3	71.851	44.991	160.244	−0.107	0.80	−35.00	31.50	12.64 ± 0.05	11.67 ± 0.05	11.25 ± 0.07	0.84	1.03	*m*S	—
16	J045414.90+450315.1	73.562	45.054	160.967	0.864	0.17	−41.28	19.00	12.79 ± 0.02	11.75 ± 0.02	11.29 ± 0.02	0.93	1.10	*e*S	6269
17	J045129.31+451852.0	72.872	45.314	160.458	0.652	0.57	−35.96	17.04	12.86 ± 0.02	11.84 ± 0.02	11.31 ± 0.02	1.04	1.10	E/S0	—
18	J045028.01+443407.6	72.617	44.569	160.916	0.037	0.70	−74.56	15.98	12.74 ± 0.02	11.79 ± 0.02	11.32 ± 0.02	0.80	1.07	E/S0	—
19	J045156.57+445815.0	72.986	44.971	160.774	0.496	0.47	−12.60	14.73	12.79 ± 0.02	11.79 ± 0.02	11.33 ± 0.02	0.94	1.05	*e*S	—
20	J045251.94+444122.5	73.216	44.690	161.095	0.443	0.56	63.37	16.94	12.90 ± 0.02	11.92 ± 0.02	11.47 ± 0.02	0.85	1.07	*e*S	—
21	J045018.46+454152.2	72.577	45.698	160.031	0.738	0.27	24.97	12.06	13.08 ± 0.02	11.99 ± 0.02	11.49 ± 0.02	1.17	1.08	E/S0	—
22	J045324.45+451127.6	73.352	45.191	160.768	0.835	0.40	29.03	12.08	12.97 ± 0.02	11.93 ± 0.02	11.50 ± 0.02	0.98	1.05	E/S0	—
23	J044753.50+443250.9	71.973	44.547	160.638	−0.328	0.10	25.00	13.10	12.88 ± 0.04	11.87 ± 0.05	11.52 ± 0.06	0.84	1.00	E/S0	—
24	J044734.77+452912.6	71.895	45.487	159.885	0.237	0.41	50.35	8.87	13.14 ± 0.02	12.05 ± 0.02	11.56 ± 0.02	1.19	1.06	E/S0	—
25	J045332.55+453232.6	73.386	45.542	160.510	1.076	0.39	−23.08	14.16	13.09 ± 0.02	12.03 ± 0.02	11.56 ± 0.02	0.98	1.11	E/S0	—

[*] v_{opt}: Spinrad 1975
[×] v_{opt}: Spinrad 1975
[+] v_{opt} = 5150 (Takata et al. 1994)

Table B – Continued

ID no.	Unique ID	RA	Dec	ℓ	b	ϵ_K	ϕ_K	r_{K20}	J_{K20}	H_{K20}	K_{K20}	$E(B\text{-}V)$	J^o-K^o	Type	v_{rad}
	ZoA	deg	deg	deg	deg		deg	$''$	mag	mag	mag	mag	mag		km s^{-1}
(1)	(2)	(3)	(4)	(5)	(6)	(7)	(8)	(9)	(10)	(11)	(12)	(13)	(14)	(15)	(16)
26	J044639.43+454052.2	71.664	45.681	159.633	0.240	0.41	85.72	12.30	13.12 ± 0.02	12.08 ± 0.02	11.57 ± 0.02	1.25	1.01	E/S0	—
27	J044730.43+454548.7	71.877	45.764	159.666	0.406	0.20	47.01	10.49	13.14 ± 0.02	12.11 ± 0.02	11.62 ± 0.02	1.25	0.98	eS	—
28	J044953.41+451613.5	72.473	45.270	160.312	0.408	0.60	−60.00	15.10	13.33 ± 0.05	12.16 ± 0.04	11.71 ± 0.06	1.01	1.18	eS	—
29	J045032.79+445411.7	72.637	44.903	160.668	0.262	0.29	−10.36	12.04	13.26 ± 0.02	12.21 ± 0.02	11.71 ± 0.02	0.92	1.15	eS	—
30	J044940.04+451119.0	72.417	45.189	160.350	0.325	0.62	−10.81	13.76	13.23 ± 0.02	12.22 ± 0.02	11.72 ± 0.02	0.98	1.09	eS	—
31	J045020.02+445348.1	72.583	44.897	160.649	0.229	0.58	−15.99	14.81	13.20 ± 0.02	12.22 ± 0.02	11.73 ± 0.02	0.95	1.06	E/S0	—
32	J045049.32+445742.3	72.706	44.962	160.655	0.337	0.36	−76.66	11.22	13.28 ± 0.02	12.26 ± 0.02	11.80 ± 0.02	0.91	1.09	E/S0	—
33	J045346.20+450747.8	73.443	45.130	160.855	0.846	0.41	7.89	15.79	13.31 ± 0.02	12.22 ± 0.02	11.80 ± 0.02	0.96	1.09	mS	—
34	J044414.05+443036.7	71.059	44.510	160.243	−0.848	0.39	28.13	12.21	13.30 ± 0.02	12.30 ± 0.02	11.81 ± 0.02	1.01	1.05	E/S0	—
35	J045147.22+450757.0	72.947	45.133	160.632	0.577	0.17	−44.96	10.23	13.21 ± 0.02	12.24 ± 0.02	11.81 ± 0.02	0.95	0.98	E/S0	—
36	J045117.73+451208.6	72.824	45.202	160.523	0.555	0.25	35.05	9.63	13.37 ± 0.02	12.35 ± 0.02	11.82 ± 0.02	1.01	1.12	E/S0	—
37	J045132.32+442920.1	72.885	44.489	161.100	0.133	0.73	−87.70	16.54	13.36 ± 0.02	12.43 ± 0.02	11.85 ± 0.02	0.76	1.18	eS	5129
38	J044918.07+445318.3	72.325	44.888	160.538	0.083	0.21	−18.37	10.40	13.23 ± 0.02	12.26 ± 0.02	11.86 ± 0.02	0.90	0.98	eS	—
39	J044941.69+452719.7	72.424	45.455	160.148	0.500	0.18	−13.54	8.04	13.42 ± 0.02	12.42 ± 0.02	11.86 ± 0.02	1.04	1.11	eS	—
40	J045021.54+450047.4	72.590	45.013	160.563	0.307	0.53	−84.10	13.27	13.43 ± 0.02	12.39 ± 0.02	11.90 ± 0.02	0.98	1.10	eS	—
41	J044558.57+441637.7	71.494	44.277	160.623	−0.764	0.55	−11.81	17.24	13.30 ± 0.02	12.31 ± 0.02	11.91 ± 0.02	0.85	1.03	eS	—
42	J045135.55+450302.9	72.898	45.051	160.673	0.499	0.50	54.65	10.20	13.39 ± 0.02	12.43 ± 0.02	11.95 ± 0.02	0.95	1.03	E/S0	—
43	J044913.04+443545.2	72.304	44.596	160.753	−0.116	0.48	4.20	9.99	13.45 ± 0.02	12.55 ± 0.02	12.14 ± 0.02	0.78	0.97	E/S0	—
44	J045005.82+453012.6	72.524	45.503	160.156	0.585	0.23	18.87	10.69	13.69 ± 0.02	12.72 ± 0.02	12.14 ± 0.02	1.09	1.08	mS	—
45	J044940.15+445844.4	72.417	44.979	160.511	0.191	0.64	7.97	14.62	13.63 ± 0.02	12.63 ± 0.02	12.17 ± 0.02	0.94	1.05	eS	—
46	J045134.83+452431.0	72.895	45.409	160.395	0.725	0.12	−70.79	10.37	13.68 ± 0.02	12.66 ± 0.02	12.18 ± 0.02	1.05	1.05	E/S0	—
47	J045217.59+443511.6	73.073	44.587	161.110	0.299	0.46	−36.63	9.46	13.53 ± 0.02	12.62 ± 0.02	12.19 ± 0.02	0.76	1.02	E/S0	—
48	J044747.17+444434.0	71.947	44.743	160.477	−0.216	0.50	10.00	12.70	13.59 ± 0.05	12.61 ± 0.06	12.20 ± 0.07	0.88	1.01	eS	—
49	J044935.63+450035.3	72.398	45.010	160.479	0.201	0.40	60.58	10.79	13.67 ± 0.02	12.65 ± 0.02	12.21 ± 0.02	0.95	1.05	eS	—
50	J044956.71+451705.5	72.486	45.285	160.307	0.425	0.17	56.59	11.24	13.81 ± 0.02	12.71 ± 0.02	12.26 ± 0.02	1.04	1.10	E/S0	—
51	J045018.81+451136.0	72.578	45.193	160.419	0.416	0.47	−47.84	10.04	13.83 ± 0.02	12.79 ± 0.02	12.28 ± 0.02	1.02	1.11	eS	—
52	J044557.04+450410.9	71.488	45.070	160.017	−0.252	0.09	−21.67	8.27	13.78 ± 0.02	12.78 ± 0.02	12.35 ± 0.02	0.98	1.01	E/S0	—
53	J044820.62+453134.0	72.086	45.526	159.942	0.364	0.51	53.15	10.89	13.84 ± 0.02	12.83 ± 0.02	12.38 ± 0.02	1.04	1.01	E/S0	—
54	J044608.05+441621.5	71.534	44.273	160.644	−0.745	0.75	−11.80	14.15	13.93 ± 0.02	12.96 ± 0.02	12.48 ± 0.02	0.84	1.09	eS	—
55	J045303.58+442506.5	73.265	44.418	161.327	0.298	0.68	−3.61	12.52	13.80 ± 0.02	12.92 ± 0.02	12.50 ± 0.02	0.78	0.97	eS	—
56	J044934.14+443426.7	72.392	44.574	160.810	−0.082	0.44	35.56	14.58	13.84 ± 0.02	12.91 ± 0.02	12.52 ± 0.02	0.76	0.99	mS	—

Table B – Continued

ID no.	Unique ID	RA	Dec	ℓ	b	ϵ_K	ϕ_K	r_{K20}	J_{K20}	H_{K20}	K_{K20}	$E(B\text{-}V)$	J^o-K^o	Type	v_{rad}
	ZoA	deg	deg	deg	deg		deg	$''$	mag	mag	mag	mag	mag		km s^{-1}
(1)	(2)	(3)	(4)	(5)	(6)	(7)	(8)	(9)	(10)	(11)	(12)	(13)	(14)	(15)	(16)
57	J045038.23+450521.6	72.659	45.089	160.535	0.393	0.36	47.90	6.84	14.07 ± 0.02	13.09 ± 0.02	12.54 ± 0.02	1.00	1.10	E/S0	—
58	J045125.48+452551.4	72.856	45.431	160.361	0.718	0.52	79.07	12.39	14.08 ± 0.02	13.04 ± 0.02	12.54 ± 0.02	1.09	1.06	mS	—
59	J044949.59+450319.7	72.457	45.055	160.470	0.262	0.20	−30.00	8.50	14.07 ± 0.07	13.03 ± 0.06	12.57 ± 0.08	0.96	1.08	E/S0	—
60	J045401.51+451426.6	73.506	45.241	160.798	0.951	0.55	−61.16	9.67	14.01 ± 0.02	13.01 ± 0.02	12.57 ± 0.02	0.98	1.02	eS	—
61	J045444.87+453116.6	73.687	45.521	160.660	1.226	0.50	51.50	13.71	13.94 ± 0.02	12.98 ± 0.02	12.57 ± 0.02	0.80	1.02	eS	—
62	J045233.08+445548.6	73.138	44.930	160.874	0.553	0.63	−57.68	8.91	14.06 ± 0.02	13.08 ± 0.02	12.59 ± 0.02	0.94	1.07	eS	—
63	J044646.93+441620.4	71.696	44.272	160.720	−0.657	0.61	−84.87	13.48	13.94 ± 0.02	12.99 ± 0.02	12.60 ± 0.02	0.74	1.01	mS	—
64	J044801.07+444319.3	72.004	44.722	160.519	−0.198	0.26	24.21	7.83	14.05 ± 0.02	13.08 ± 0.02	12.64 ± 0.02	0.86	1.04	E/S0	—
65	J045040.23+445701.0	72.668	44.950	160.646	0.309	0.70	−67.23	14.57	14.07 ± 0.02	13.09 ± 0.02	12.68 ± 0.02	0.92	0.99	mS	—
66	J044409.43+443700.4	71.039	44.617	160.153	−0.788	0.40	−51.65	10.30	14.22 ± 0.02	13.18 ± 0.02	12.70 ± 0.02	1.09	1.06	mS	—
67	J044902.91+445639.9	72.262	44.944	160.467	0.085	0.07	−89.11	8.41	14.11 ± 0.02	13.16 ± 0.02	12.70 ± 0.02	0.90	1.03	eS	—
68	J044927.08+450121.8	72.363	45.023	160.452	0.190	0.29	−83.90	7.96	14.22 ± 0.02	13.18 ± 0.02	12.73 ± 0.02	0.95	1.08	E/S0	—
69	J045429.83+444425.9	73.624	44.741	161.239	0.700	0.38	−74.39	7.18	14.23 ± 0.02	13.23 ± 0.02	12.75 ± 0.02	0.87	1.10	eS	—
70	J045156.51+450314.5	72.985	45.054	160.710	0.548	0.40	30.50	10.67	14.16 ± 0.02	13.23 ± 0.02	12.80 ± 0.02	0.94	0.96	mS	4523
71	J044642.74+444225.2	71.678	44.707	160.381	−0.385	0.02	−69.65	5.85	14.25 ± 0.02	13.26 ± 0.02	12.80 ± 0.02	0.92	1.06	eS	—
72	J045031.44+453451.2	72.631	45.581	160.145	0.692	0.43	−20.20	8.32	14.37 ± 0.02	13.35 ± 0.02	12.86 ± 0.02	1.20	0.99	eS	—
73	J044741.94+445903.4	71.925	44.984	160.282	−0.072	0.36	17.96	8.27	14.24 ± 0.02	13.30 ± 0.02	12.87 ± 0.02	0.86	1.01	eS	—
74	J045030.71+442816.0	72.628	44.471	160.997	−0.019	0.35	45.97	8.77	14.15 ± 0.02	13.25 ± 0.02	12.87 ± 0.02	0.79	0.94	eS	—
75	J045149.06+450924.8	72.954	45.157	160.616	0.597	0.22	44.85	7.22	14.29 ± 0.02	13.33 ± 0.02	12.87 ± 0.02	0.93	1.03	E/S0	—
76	J044615.88+450530.3	71.566	45.092	160.036	−0.195	0.65	62.54	9.64	14.26 ± 0.02	13.44 ± 0.02	12.91 ± 0.02	0.94	0.94	eS	—
77	J044752.80+450202.3	71.970	45.034	160.265	−0.015	0.40	−40.00	9.50	14.26 ± 0.08	13.35 ± 0.08	12.91 ± 0.09	0.86	0.98	E/S0	—
78	J045005.99+444129.8	72.525	44.692	160.780	0.066	0.57	−84.01	7.73	14.31 ± 0.02	13.41 ± 0.02	12.97 ± 0.02	0.82	0.98	eS	—
79	J044707.90+442944.4	71.783	44.496	160.590	−0.465	0.10	−69.40	7.97	14.43 ± 0.02	13.54 ± 0.02	12.98 ± 0.02	0.78	1.11	E/S0	—
80	J044918.88+454737.1	72.329	45.794	159.846	0.666	0.21	−51.00	9.01	14.60 ± 0.02	13.56 ± 0.02	12.98 ± 0.02	1.14	1.12	mS	—
81	J045418.02+453951.7	73.575	45.664	160.499	1.255	0.39	49.59	9.30	14.35 ± 0.02	13.41 ± 0.02	13.00 ± 0.02	0.88	0.96	mS	—
82	J045353.83+443238.8	73.474	44.544	161.324	0.494	0.37	37.88	8.88	14.45 ± 0.02	13.51 ± 0.02	13.02 ± 0.02	0.85	1.07	eS	—
83	J045146.37+452706.8	72.943	45.452	160.384	0.778	0.59	79.33	8.71	14.54 ± 0.02	13.53 ± 0.02	13.04 ± 0.02	1.13	1.01	eS	—
84	J044520.92+454430.7	71.337	45.742	159.440	0.110	0.77	24.83	14.61	14.94 ± 0.02	13.68 ± 0.02	13.05 ± 0.02	1.28	1.33	mS	5134
85	J045206.26+451041.6	73.026	45.178	160.632	0.649	0.23	−75.26	6.58	14.51 ± 0.02	13.48 ± 0.02	13.05 ± 0.02	0.90	1.07	E/S0	—
86	J044859.13+450201.1	72.246	45.034	160.391	0.134	0.22	−23.15	6.11	14.55 ± 0.02	13.54 ± 0.02	13.06 ± 0.02	0.93	1.08	E/S0	—
87	J045022.58+451600.9	72.594	45.267	160.370	0.472	0.26	65.62	6.78	14.66 ± 0.02	13.54 ± 0.02	13.06 ± 0.02	1.03	1.16	E/S0	—

Table B – Continued

ID no.	Unique ID	RA	Dec	ℓ	b	ϵ_K	ϕ_K	r_{K20}	J_{K20}	H_{K20}	K_{K20}	$E(B\text{-}V)$	$J^o{-}K^o$	Type	v_{rad}
	ZoA	deg	deg	deg	deg		deg	$''$	mag	mag	mag	mag	mag		km s^{-1}
(1)	(2)	(3)	(4)	(5)	(6)	(7)	(8)	(9)	(10)	(11)	(12)	(13)	(14)	(15)	(16)
88	J044848.38+450140.8	72.202	45.028	160.375	0.106	0.48	−43.50	8.56	14.60 ± 0.02	13.54 ± 0.02	13.11 ± 0.02	0.90	1.09	mS	—
89	J044941.44+445807.9	72.423	44.969	160.521	0.188	0.21	−34.30	6.52	14.52 ± 0.02	13.55 ± 0.02	13.12 ± 0.02	0.94	1.00	E/S0	—
90	J044922.34+444427.2	72.343	44.741	160.660	−0.002	0.08	−15.60	6.15	14.55 ± 0.02	13.59 ± 0.02	13.17 ± 0.02	0.84	1.01	eS	—
91	J044812.49+450920.1	72.052	45.156	160.210	0.107	0.24	−45.33	7.28	14.60 ± 0.02	13.61 ± 0.02	13.20 ± 0.02	0.94	0.99	eS	—
92	J044743.67+445439.8	71.932	44.911	160.342	−0.115	0.41	−69.81	7.60	14.56 ± 0.02	13.68 ± 0.02	13.21 ± 0.02	0.84	0.98	eS	—
93	J045131.32+450558.1	72.880	45.099	160.627	0.520	0.03	−16.62	6.54	14.74 ± 0.02	13.72 ± 0.02	13.25 ± 0.02	0.95	1.07	E/S0	—
94	J044944.65+452304.9	72.436	45.385	160.208	0.462	0.37	−41.69	7.31	14.70 ± 0.02	13.70 ± 0.02	13.26 ± 0.02	1.06	0.99	eS	—
95	J044933.20+445558.6	72.388	44.933	160.533	0.146	0.10	−56.04	4.90	14.75 ± 0.02	13.76 ± 0.02	13.28 ± 0.02	0.94	1.06	E/S0	—
96	J044935.99+445213.7	72.400	44.870	160.586	0.112	0.24	2.46	6.83	14.75 ± 0.02	13.73 ± 0.02	13.30 ± 0.02	0.93	1.05	E/S0	—
97	J044943.68+443245.1	72.432	44.546	160.850	−0.078	0.16	−59.70	5.72	14.63 ± 0.02	13.73 ± 0.02	13.35 ± 0.02	0.75	0.97	eS	—
98	J045216.50+441218.2	73.069	44.205	161.403	0.055	0.27	−3.60	6.37	14.72 ± 0.02	13.77 ± 0.02	13.35 ± 0.02	0.63	1.10	E/S0	—
99	J044947.45+450944.5	72.448	45.162	160.384	0.325	0.43	−44.49	7.29	14.89 ± 0.02	13.88 ± 0.02	13.37 ± 0.02	0.98	1.10	eS	—
100	J044417.15+443615.4	71.071	44.604	160.178	−0.779	0.50	−50.00	9.40	14.98 ± 0.11	13.80 ± 0.09	13.46 ± 0.12	1.09	1.04	mS	—
101	J045226.36+451011.7	73.110	45.170	160.676	0.690	0.39	21.47	6.53	14.89 ± 0.02	13.93 ± 0.02	13.47 ± 0.02	0.87	1.05	E/S0	—
102	J045216.79+455402.2	73.070	45.901	160.093	1.132	0.52	−17.24	7.05	14.93 ± 0.02	13.96 ± 0.02	13.49 ± 0.02	1.02	1.00	mS	—
103	J045301.01+442921.2	73.254	44.489	161.267	0.337	0.39	34.50	7.43	14.92 ± 0.02	13.97 ± 0.02	13.50 ± 0.02	0.80	1.08	mS	—
104	J045314.91+452642.6	73.312	45.445	160.553	0.974	0.49	−74.74	6.44	14.98 ± 0.02	13.98 ± 0.02	13.54 ± 0.02	0.98	1.02	E/S0	—
105	J044650.13+452342.0	71.709	45.395	159.871	0.078	0.45	65.44	7.23	15.07 ± 0.02	14.04 ± 0.02	13.55 ± 0.02	1.13	1.03	eS	—
106	J045004.69+450036.1	72.520	45.010	160.533	0.267	0.34	31.33	4.94	15.09 ± 0.02	14.08 ± 0.02	13.57 ± 0.02	0.97	1.10	E/S0	—
107	J045100.26+445855.4	72.751	44.982	160.659	0.375	0.24	36.21	4.72	15.04 ± 0.02	14.05 ± 0.02	13.62 ± 0.02	0.91	1.03	E/S0	—
108	J044959.35+445647.7	72.497	44.947	160.572	0.214	0.33	−53.30	6.69	15.11 ± 0.02	14.13 ± 0.02	13.65 ± 0.02	0.97	1.04	mS	—
109	J045432.63+451846.8	73.636	45.313	160.799	1.067	0.16	−0.60	3.03	15.19 ± 0.02	14.23 ± 0.02	13.67 ± 0.02	0.90	1.14	E/S0	—
110	J045445.42+453911.3	73.689	45.653	160.560	1.310	0.48	−39.85	9.48	14.87 ± 0.02	14.01 ± 0.02	13.73 ± 0.03	0.84	0.77	mS	4941
111	J045143.42+454722.1	72.931	45.789	160.118	0.987	0.26	−66.54	3.51	15.37 ± 0.02	14.40 ± 0.02	13.77 ± 0.02	1.34	1.02	E/S0	—
112	J044900.93+441937.0	72.254	44.327	160.936	−0.316	0.69	−85.32	9.15	15.20 ± 0.02	14.27 ± 0.02	13.81 ± 0.03	0.64	1.11	mS	6332
113	J044555.95+444549.4	71.483	44.764	160.248	−0.453	0.24	70.62	6.78	15.19 ± 0.02	14.23 ± 0.02	13.81 ± 0.03	0.99	0.95	mS	—
114	J045403.78+443621.7	73.516	44.606	161.294	0.556	0.49	−43.64	6.81	15.12 ± 0.02	14.20 ± 0.02	13.81 ± 0.02	0.87	0.94	mS	—
115	J044823.57+451244.2	72.098	45.212	160.187	0.169	0.03	41.98	5.03	15.23 ± 0.02	14.28 ± 0.02	13.82 ± 0.02	0.98	0.99	mS	—
116	J045105.62+443545.0	72.773	44.596	160.970	0.140	0.05	38.79	5.25	14.93 ± 0.02	14.18 ± 0.02	13.87 ± 0.03	0.77	0.73	mS	5044
117	J045156.82+453619.8	72.987	45.606	160.284	0.900	0.12	−0.68	4.67	15.62 ± 0.02	14.53 ± 0.02	13.88 ± 0.02	1.62	1.04	E/S0	—
118	J044920.79+450159.4	72.337	45.033	160.433	0.183	0.50	−60.00	7.60	15.25 ± 0.13	14.00 ± 0.09	13.89 ± 0.14	0.95	0.95	mS	—

Table B – Continued

ID no.	Unique ID	RA	Dec	ℓ	b	ϵ_K	ϕ_K	r_{K20}	J_{K20}	H_{K20}	K_{K20}	$E(B\text{-}V)$	J^o-K^o	Type	v_{rad}
	ZoA	deg	deg	deg	deg		deg	$''$	mag	mag	mag	mag	mag		km s^{-1}
(1)	(2)	(3)	(4)	(5)	(6)	(7)	(8)	(9)	(10)	(11)	(12)	(13)	(14)	(15)	(16)
119	J045029.63+441012.4	72.623	44.170	161.226	−0.214	0.15	2.40	6.40	15.15 ± 0.02	14.31 ± 0.02	13.92 ± 0.03	0.64	0.96	mS	—
120	J044706.52+451102.1	71.777	45.184	160.063	−0.022	0.07	−35.59	3.95	15.36 ± 0.02	14.40 ± 0.02	13.94 ± 0.02	0.94	1.01	E/S0	—
121	J044950.94+454506.7	72.462	45.752	159.938	0.711	0.14	−35.38	4.73	15.53 ± 0.02	14.48 ± 0.02	13.94 ± 0.02	1.15	1.09	E/S0	—
122	J044434.42+445034.2	71.143	44.843	160.031	−0.584	0.10	9.12	3.65	15.44 ± 0.02	14.40 ± 0.02	13.96 ± 0.02	1.11	1.01	E/S0	—
123	J044946.26+450747.6	72.443	45.130	160.406	0.302	0.49	24.10	6.81	15.45 ± 0.02	14.37 ± 0.02	13.97 ± 0.03	0.98	1.07	mS	—
124	J044658.40+452255.0	71.743	45.382	159.896	0.088	0.07	−35.86	4.02	15.61 ± 0.02	14.62 ± 0.02	13.99 ± 0.02	1.11	1.14	E/S0	—
125	J044816.56+451604.5	72.069	45.268	160.131	0.189	0.01	−39.80	4.12	15.38 ± 0.02	14.43 ± 0.02	14.00 ± 0.02	1.02	0.94	E/S0	—
126	J045042.89+445937.4	72.679	44.994	160.618	0.343	0.32	−63.47	5.81	15.48 ± 0.02	14.43 ± 0.02	14.00 ± 0.02	0.93	1.07	mS	—
127	J044403.24+443827.5	71.014	44.641	160.123	−0.786	0.00	90.00	5.90	15.56 ± 0.16	14.36 ± 0.13	14.02 ± 0.17	1.10	1.06	mS	—
128	J045021.00+451216.6	72.587	45.205	160.414	0.428	0.26	−72.94	5.67	15.53 ± 0.02	14.49 ± 0.02	14.02 ± 0.02	1.02	1.07	mS	—
129	J045029.29+460723.4	72.622	46.123	159.724	1.034	0.28	49.67	5.21	15.57 ± 0.02	14.62 ± 0.02	14.02 ± 0.02	0.99	1.13	E/S0	—
130	J044646.85+452209.9	71.695	45.369	159.884	0.054	0.09	−26.10	4.14	15.59 ± 0.02	14.60 ± 0.02	14.03 ± 0.02	1.10	1.09	E/S0	—
131	J045419.04+452229.0	73.579	45.375	160.726	1.075	0.20	72.14	5.28	15.48 ± 0.02	14.53 ± 0.02	14.03 ± 0.02	0.93	1.04	mS	—
132	J045416.62+452530.8	73.569	45.425	160.682	1.102	0.00	90.00	5.00	15.42 ± 0.14	14.49 ± 0.14	14.07 ± 0.16	0.90	0.96	eS	—
133	J044721.08+450806.7	71.838	45.135	160.128	−0.021	0.25	−58.10	5.70	15.47 ± 0.02	14.50 ± 0.02	14.09 ± 0.03	0.90	0.99	mS	—
134	J045002.01+450215.3	72.508	45.038	160.507	0.278	0.48	55.19	6.12	15.54 ± 0.02	14.54 ± 0.02	14.09 ± 0.02	0.98	1.03	eS	—
135	J045541.23+445953.2	73.922	44.998	161.171	1.026	0.33	−54.60	5.30	15.60 ± 0.02	14.64 ± 0.02	14.11 ± 0.02	0.90	1.11	eS	—
136	J044802.83+452237.9	72.012	45.377	160.022	0.229	0.17	22.56	4.32	15.71 ± 0.02	14.76 ± 0.02	14.12 ± 0.02	1.07	1.13	E/S0	—
137	J044524.63+451918.2	71.353	45.322	159.764	−0.160	0.02	−32.18	4.01	15.60 ± 0.02	14.71 ± 0.02	14.13 ± 0.03	1.14	0.98	mS	6830
138	J044908.53+450705.9	72.286	45.118	160.344	0.209	0.12	26.00	5.19	15.57 ± 0.02	14.58 ± 0.02	14.14 ± 0.03	0.96	1.02	mS	—
139	J044755.58+450438.2	71.982	45.077	160.237	0.019	0.43	−62.81	5.82	15.52 ± 0.02	14.55 ± 0.02	14.15 ± 0.03	0.88	1.00	mS	—
140	J045029.48+450139.1	72.623	45.028	160.567	0.334	0.15	−24.88	3.98	15.66 ± 0.02	14.65 ± 0.02	14.15 ± 0.02	0.97	1.09	Irr	—
141	J045026.25+445346.6	72.609	44.896	160.661	0.243	0.04	42.27	4.30	15.56 ± 0.02	14.64 ± 0.02	14.18 ± 0.02	0.93	0.98	E/S0	—
142	J044616.70+440932.4	71.570	44.159	160.748	−0.799	0.17	26.77	4.30	15.52 ± 0.02	14.62 ± 0.02	14.19 ± 0.03	0.79	0.99	mS	—
143	J044632.01+440858.6	71.633	44.150	160.784	−0.770	0.00	90.00	5.00	15.53 ± 0.14	14.43 ± 0.04	14.21 ± 0.17	0.75	1.00	eS	—
144	J044603.60+444430.9	71.515	44.742	160.279	−0.450	0.09	−5.20	4.19	15.61 ± 0.02	14.62 ± 0.02	14.24 ± 0.03	0.99	0.93	mS	—
145	J044357.81+443721.5	70.991	44.623	160.126	−0.810	0.48	81.34	5.71	15.74 ± 0.02	14.74 ± 0.02	14.25 ± 0.03	1.09	1.03	mS	—
146	J045159.93+451925.2	73.000	45.324	160.508	0.728	0.58	8.91	6.35	15.66 ± 0.02	14.69 ± 0.02	14.25 ± 0.03	0.99	0.98	eS	—
147	J045229.45+452451.7	73.123	45.414	160.493	0.852	0.59	−19.33	6.61	15.66 ± 0.02	14.72 ± 0.02	14.25 ± 0.02	0.98	0.99	mS	—
148	J044728.19+450836.8	71.867	45.144	160.135	0.000	0.49	88.14	6.20	15.63 ± 0.02	14.71 ± 0.02	14.26 ± 0.03	0.95	0.95	ℓS	—
149	J045409.86+445915.6	73.541	44.988	161.010	0.810	0.42	−78.78	6.35	15.66 ± 0.02	14.73 ± 0.02	14.28 ± 0.03	0.91	1.00	E/S0	—

Table B – Continued

ID no.	Unique ID	RA	Dec	ℓ	b	ϵ_K	ϕ_K	r_{K20}	J_{K20}	H_{K20}	K_{K20}	$E(B\text{-}V)$	J^o-K^o	Type	v_{rad}
	ZoA	deg	deg	deg	deg		deg	$''$	mag	mag	mag	mag	mag		km s^{-1}
(1)	(2)	(3)	(4)	(5)	(6)	(7)	(8)	(9)	(10)	(11)	(12)	(13)	(14)	(15)	(16)
150	J044944.04+452717.6	72.434	45.455	160.153	0.505	0.28	−69.33	3.95	15.88 ± 0.02	14.92 ± 0.02	14.32 ± 0.02	1.04	1.11	E/S0	—
151	J044456.88+453304.0	71.237	45.551	159.537	−0.072	0.04	−58.90	4.28	16.03 ± 0.03	14.95 ± 0.02	14.33 ± 0.03	1.35	1.12	E/S0	—
152	J045213.66+455728.1	73.057	45.958	160.043	1.161	0.38	−41.73	4.79	15.89 ± 0.02	14.96 ± 0.02	14.35 ± 0.03	1.04	1.09	E/S0	—
153	J045253.13+443406.9	73.221	44.569	161.191	0.369	0.36	78.70	5.33	15.76 ± 0.02	14.84 ± 0.02	14.36 ± 0.03	0.78	1.05	ℓS	—
154	J044744.15+441950.0	71.934	44.331	160.786	−0.489	0.60	−18.30	6.04	15.63 ± 0.02	14.83 ± 0.02	14.42 ± 0.03	0.70	0.90	ℓS	4878
155	J044434.53+452801.4	71.144	45.467	159.558	−0.176	0.19	−44.80	3.98	16.13 ± 0.02	15.09 ± 0.02	14.44 ± 0.03	1.30	1.13	mS	—
156	J045238.00+453139.1	73.158	45.528	160.421	0.943	0.30	16.90	3.91	15.94 ± 0.02	14.93 ± 0.02	14.44 ± 0.02	1.17	0.99	eS	—
157	J044926.79+445532.2	72.362	44.926	160.526	0.127	0.67	−51.10	7.25	15.81 ± 0.02	14.92 ± 0.02	14.45 ± 0.03	0.92	0.96	mS	—
158	J044651.22+442147.3	71.713	44.363	160.659	−0.588	0.06	−23.49	4.07	15.86 ± 0.03	15.03 ± 0.02	14.48 ± 0.03	0.73	1.07	E/S0	—
159	J045216.28+451657.3	73.068	45.283	160.570	0.738	0.20	34.80	4.58	15.96 ± 0.03	15.02 ± 0.02	14.52 ± 0.03	0.92	1.04	mS	—
160	J044858.75+441329.9	72.245	44.225	161.010	−0.387	0.47	−82.16	4.88	15.89 ± 0.02	14.98 ± 0.02	14.57 ± 0.03	0.67	1.03	ℓS	—
161	J044947.40+444454.6	72.447	44.749	160.701	0.060	0.67	16.72	6.49	15.96 ± 0.03	14.99 ± 0.02	14.59 ± 0.03	0.86	1.00	mS	—
162	J045224.39+451948.4	73.102	45.330	160.548	0.787	0.39	−64.60	4.15	16.01 ± 0.02	15.11 ± 0.02	14.60 ± 0.03	0.94	1.01	E/S0	—
163	J045012.16+445802.4	72.551	44.967	160.580	0.256	0.57	18.53	6.47	16.12 ± 0.03	15.08 ± 0.02	14.61 ± 0.03	0.97	1.09	eS	—
164	J044621.16+441634.4	71.588	44.276	160.667	−0.713	0.49	−5.56	4.98	15.90 ± 0.02	15.00 ± 0.02	14.62 ± 0.03	0.81	0.93	mS	—
165	J045532.82+450602.8	73.887	45.101	161.075	1.071	0.24	−51.61	3.82	16.05 ± 0.02	15.09 ± 0.02	14.63 ± 0.03	0.91	1.03	mS	—
166	J044858.41+451309.8	72.243	45.219	160.248	0.252	0.10	−46.62	4.23	16.21 ± 0.03	15.16 ± 0.02	14.69 ± 0.03	0.96	1.11	mS	—
167	J045011.73+445955.1	72.549	44.999	160.555	0.275	0.41	51.90	4.58	16.12 ± 0.02	15.12 ± 0.02	14.70 ± 0.03	0.98	1.00	mS	—
168	J044651.60+455551.6	71.715	45.931	159.465	0.428	0.30	−7.58	4.66	16.34 ± 0.03	15.33 ± 0.03	14.71 ± 0.03	1.22	1.11	eS	—
169	J044739.96+443348.7	71.917	44.564	160.600	−0.348	0.38	46.20	5.61	16.07 ± 0.03	15.09 ± 0.02	14.72 ± 0.03	0.84	0.98	Irr	—
170	J044406.51+445621.7	71.027	44.939	159.904	−0.584	0.33	10.47	4.93	16.27 ± 0.03	15.19 ± 0.02	14.75 ± 0.03	1.15	1.02	mS	—
171	J044541.16+454528.0	71.421	45.758	159.464	0.160	0.19	−38.51	3.12	16.40 ± 0.03	15.37 ± 0.02	14.75 ± 0.03	1.26	1.11	E/S0	—
172	J044645.56+450429.6	71.690	45.075	160.106	−0.140	0.36	84.91	5.14	16.07 ± 0.03	15.12 ± 0.02	14.76 ± 0.03	0.88	0.94	eS	—
173	J045255.84+454914.2	73.233	45.821	160.227	1.169	0.22	−59.55	3.79	16.14 ± 0.03	15.17 ± 0.02	14.76 ± 0.03	0.96	0.97	eS	—
174	J045251.64+441648.4	73.215	44.280	161.411	0.183	0.25	−14.71	3.83	15.99 ± 0.02	15.11 ± 0.02	14.77 ± 0.03	0.66	0.94	E/S0	—
175	J044708.49+450527.2	71.785	45.091	160.137	−0.078	0.09	75.04	3.10	16.07 ± 0.02	15.13 ± 0.02	14.79 ± 0.03	0.88	0.90	E/S0	—
176	J045433.21+445344.2	73.638	44.896	161.124	0.806	0.22	−27.96	3.42	16.30 ± 0.03	15.34 ± 0.02	14.80 ± 0.03	0.89	1.12	E/S0	—
177	J045441.39+451904.9	73.672	45.318	160.811	1.090	0.35	−37.70	3.06	16.31 ± 0.02	15.59 ± 0.02	14.81 ± 0.03	0.89	1.11	eS	—
178	J044838.24+445640.2	72.159	44.945	160.420	0.029	0.09	−68.89	3.45	16.11 ± 0.02	15.20 ± 0.02	14.82 ± 0.03	0.86	0.92	E/S0	—
179	J044614.90+452745.3	71.562	45.463	159.753	0.043	0.29	13.74	3.22	16.50 ± 0.03	15.47 ± 0.02	14.85 ± 0.03	1.23	1.11	mS	—
180	J045013.36+440839.0	72.556	44.144	161.210	−0.270	0.44	79.01	4.57	15.91 ± 0.02	15.21 ± 0.02	14.87 ± 0.03	0.63	0.78	Irr	5547

Table B – Continued

ID no.	Unique ID	RA	Dec	ℓ	b	ϵ_K	ϕ_K	r_{K20}	J_{K20}	H_{K20}	K_{K20}	$E(B\text{-}V)$	J^o-K^o	Type	v_{rad}
	ZoA	deg	deg	deg	deg		deg	$''$	mag	mag	mag	mag	mag		km s^{-1}
(1)	(2)	(3)	(4)	(5)	(6)	(7)	(8)	(9)	(10)	(11)	(12)	(13)	(14)	(15)	(16)
181	J044938.32+435622.7	72.410	43.940	161.305	−0.479	0.07	−73.58	3.12	16.23 ± 0.03	15.36 ± 0.03	14.89 ± 0.03	0.62	1.07	E/S0	—
182	J044953.62+450543.4	72.473	45.095	160.447	0.296	0.12	82.40	3.15	16.38 ± 0.02	15.38 ± 0.02	14.90 ± 0.03	0.99	1.05	mS	—
183	J045123.45+460416.4	72.848	46.071	159.863	1.121	0.47	−66.91	4.71	16.38 ± 0.03	15.37 ± 0.02	14.90 ± 0.03	1.02	1.04	ℓS	—
184	J045440.78+445807.9	73.670	44.969	161.082	0.869	0.23	80.85	2.66	16.37 ± 0.02	15.44 ± 0.02	14.90 ± 0.03	0.91	1.07	E/S0	—
185	J044921.23+460126.8	72.338	46.024	159.674	0.820	0.33	6.21	3.62	16.49 ± 0.03	15.39 ± 0.03	14.92 ± 0.03	1.17	1.07	Irr	—
186	J044738.78+450532.7	71.912	45.092	160.194	−0.009	0.21	−64.50	3.95	16.35 ± 0.03	15.35 ± 0.02	14.94 ± 0.03	0.87	1.03	ℓS	—
187	J044855.57+443933.7	72.232	44.659	160.671	−0.115	0.72	4.90	8.79	16.39 ± 0.03	15.49 ± 0.03	14.94 ± 0.04	0.80	1.10	mS	—
188	J044543.46+450440.7	71.431	45.078	159.985	−0.277	0.36	−80.84	4.44	16.34 ± 0.03	15.36 ± 0.02	14.95 ± 0.03	1.03	0.95	ℓS	—
189	J044952.70+451451.0	72.470	45.247	160.328	0.392	0.24	65.67	4.62	16.50 ± 0.03	15.57 ± 0.03	14.98 ± 0.03	1.00	1.09	Irr	—
190	J044957.62+440316.6	72.490	44.055	161.254	−0.361	0.33	11.46	4.17	16.18 ± 0.03	15.36 ± 0.02	14.98 ± 0.03	0.64	0.93	ℓS	—
191	J044810.67+444742.0	72.044	44.795	160.482	−0.129	0.38	32.80	3.89	16.40 ± 0.03	15.46 ± 0.03	14.99 ± 0.04	0.82	1.05	mS	—
192	J044856.82+444953.0	72.237	44.831	160.542	−0.002	0.09	75.80	3.55	16.35 ± 0.03	15.37 ± 0.03	15.03 ± 0.03	0.83	0.96	ℓS	—
193	J044507.40+450214.4	71.281	45.037	159.947	−0.384	0.34	−30.50	4.18	16.51 ± 0.03	15.52 ± 0.03	15.05 ± 0.03	1.12	0.98	ℓS	—
194	J045420.33+451848.0	73.585	45.313	160.776	1.039	0.61	53.91	5.80	16.43 ± 0.03	15.50 ± 0.02	15.05 ± 0.03	0.92	0.98	eS	—
195	J045443.36+444708.1	73.681	44.786	161.229	0.760	0.47	−58.34	4.83	16.47 ± 0.03	15.55 ± 0.03	15.05 ± 0.04	0.88	1.03	mS	—
196	J044955.20+451139.7	72.480	45.194	160.374	0.363	0.03	−6.91	3.08	16.45 ± 0.03	15.47 ± 0.02	15.07 ± 0.03	0.99	0.96	ℓS	—
197	J044737.90+451002.9	71.908	45.167	160.135	0.037	0.23	34.62	2.81	16.59 ± 0.03	15.85 ± 0.03	15.09 ± 0.03	0.94	1.09	ℓS	—
198	J044852.61+445740.8	72.219	44.961	160.434	0.073	0.23	−14.44	3.24	16.47 ± 0.03	15.51 ± 0.02	15.10 ± 0.03	0.89	0.98	ℓS	—
199	J044547.35+454302.2	71.447	45.717	159.507	0.148	0.61	43.30	5.75	16.72 ± 0.03	15.77 ± 0.03	15.12 ± 0.04	1.27	1.05	eS	—
200	J044622.17+453307.3	71.592	45.552	159.698	0.117	0.46	−73.56	4.31	16.77 ± 0.03	15.76 ± 0.03	15.16 ± 0.04	1.28	1.06	ℓS	—
201	J044545.92+444901.9	71.441	44.817	160.188	−0.441	0.11	67.60	4.00	16.62 ± 0.03	15.75 ± 0.03	15.21 ± 0.04	1.05	0.95	ℓS	5134
202	J045012.70+453746.5	72.553	45.630	160.072	0.681	0.21	−58.70	3.14	16.78 ± 0.03	15.76 ± 0.03	15.21 ± 0.03	1.14	1.08	ℓS	—
203	J045004.97+450154.3	72.521	45.032	160.517	0.281	0.34	−22.89	3.77	16.67 ± 0.03	15.69 ± 0.02	15.24 ± 0.03	0.97	1.01	ℓS	—
204	J044617.48+452600.3	71.573	45.433	159.780	0.030	0.23	−8.24	4.19	16.87 ± 0.04	15.83 ± 0.03	15.28 ± 0.04	1.20	1.07	Irr	—
205	J045311.77+453648.0	73.299	45.613	160.417	1.074	0.18	22.04	3.19	16.73 ± 0.03	15.73 ± 0.02	15.31 ± 0.03	1.10	0.94	Irr	—
206	J045329.73+443729.2	73.374	44.625	161.216	0.489	0.61	73.06	4.40	16.66 ± 0.03	15.71 ± 0.02	15.32 ± 0.04	0.85	0.97	mS	—
207	J044445.84+444702.1	71.191	44.784	160.097	−0.597	0.20	10.23	3.97	16.90 ± 0.04	15.94 ± 0.03	15.33 ± 0.05	1.11	1.09	Irr	—
208	J045127.65+450922.6	72.865	45.156	160.577	0.548	0.56	56.41	4.66	16.82 ± 0.03	15.88 ± 0.03	15.35 ± 0.03	0.97	1.06	mS	—
209	J044955.57+454444.8	72.482	45.746	159.951	0.717	0.47	17.14	3.51	17.00 ± 0.03	16.01 ± 0.03	15.42 ± 0.03	1.16	1.09	ℓS	—
210	J044437.62+443619.0	71.157	44.605	160.217	−0.732	0.28	25.70	3.64	16.93 ± 0.03	15.90 ± 0.03	15.44 ± 0.04	1.04	1.04	Irr	—
211	J045330.45+444657.0	73.377	44.783	161.095	0.590	0.53	0.35	4.16	16.82 ± 0.03	15.84 ± 0.03	15.44 ± 0.04	0.97	0.96	eS	—

Table B – Continued

ID no.	Unique ID	RA	Dec	ℓ	b	ϵ_K	ϕ_K	r_{K20}	J_{K20}	H_{K20}	K_{K20}	$E(B\text{-}V)$	J^o-K^o	Type	v_{rad}
	ZoA	deg	deg	deg	deg		deg	$''$	mag	mag	mag	mag	mag		km s^{-1}
(1)	(2)	(3)	(4)	(5)	(6)	(7)	(8)	(9)	(10)	(11)	(12)	(13)	(14)	(15)	(16)
212	J044756.88+442015.1	71.987	44.338	160.805	−0.456	0.20	66.40	3.21	16.75 ± 0.03	15.89 ± 0.03	15.45 ± 0.04	0.69	1.00	Irr	—
213	J044958.64+450152.9	72.494	45.031	160.505	0.267	0.31	−62.00	2.79	16.90 ± 0.03	15.87 ± 0.02	15.45 ± 0.03	0.96	1.03	E/S0	—
214	J045225.84+451456.9	73.108	45.249	160.614	0.739	0.00	−7.64	3.17	16.85 ± 0.03	15.87 ± 0.03	15.48 ± 0.04	0.90	0.99	Irr	—
215	J044531.48+443550.4	71.381	44.597	160.327	−0.617	0.12	−17.07	2.91	16.96 ± 0.03	15.98 ± 0.03	15.49 ± 0.04	1.04	1.02	ℓS	—
216	J044638.07+444609.2	71.659	44.769	160.324	−0.355	0.53	−89.04	4.01	17.01 ± 0.03	16.05 ± 0.03	15.53 ± 0.04	0.91	1.09	eS	—
217	J044744.40+445626.1	71.935	44.941	160.321	−0.095	0.18	−5.80	2.80	16.89 ± 0.03	15.99 ± 0.03	15.53 ± 0.04	0.85	1.00	Irr	—
218	J044922.06+453019.4	72.342	45.505	160.073	0.488	0.01	42.10	2.83	16.98 ± 0.03	16.04 ± 0.03	15.54 ± 0.04	0.99	1.01	Irr	—
219	J045057.35+452532.4	72.739	45.426	160.312	0.651	0.14	9.90	3.04	17.04 ± 0.03	15.98 ± 0.03	15.54 ± 0.04	1.08	1.03	ℓS	—
220	J044957.27+460315.1	72.489	46.054	159.720	0.920	0.44	19.55	4.28	16.93 ± 0.03	16.07 ± 0.03	15.56 ± 0.04	1.12	0.89	ℓS	4942
221	J045241.41+452024.6	73.173	45.340	160.572	0.832	0.05	−62.10	2.92	16.91 ± 0.03	16.01 ± 0.03	15.56 ± 0.04	0.93	0.95	ℓS	—
222	J044854.97+453243.7	72.229	45.545	159.991	0.454	0.06	−44.99	3.28	16.88 ± 0.03	16.01 ± 0.03	15.57 ± 0.04	0.97	0.89	Irr	—
223	J045243.81+443819.6	73.183	44.639	161.119	0.393	0.24	−26.00	3.20	16.89 ± 0.03	16.05 ± 0.03	15.57 ± 0.04	0.81	0.97	ℓS	—
224	J045338.36+452459.0	73.410	45.416	160.619	1.009	0.12	−50.48	2.87	17.07 ± 0.03	16.22 ± 0.03	15.57 ± 0.03	0.92	1.10	Irr	—
225	J044959.00+442427.5	72.496	44.408	160.985	−0.132	0.34	39.37	2.94	16.85 ± 0.03	16.17 ± 0.03	15.62 ± 0.05	0.69	0.93	Irr	—
226	J045143.42+445733.8	72.931	44.959	160.758	0.458	0.23	74.31	3.34	16.98 ± 0.03	16.10 ± 0.03	15.62 ± 0.04	0.94	0.95	Irr	—
227	J044812.83+445407.6	72.053	44.902	160.404	−0.055	0.14	32.10	3.16	17.03 ± 0.04	16.17 ± 0.03	15.64 ± 0.04	0.84	1.03	ℓS	—
228	J045038.65+445618.6	72.661	44.938	160.652	0.298	0.15	−86.90	2.79	17.02 ± 0.03	16.02 ± 0.03	15.65 ± 0.04	0.92	0.97	ℓS	—
229	J045453.21+444522.8	73.722	44.756	161.270	0.764	0.22	48.70	3.10	17.01 ± 0.04	16.09 ± 0.03	15.70 ± 0.05	0.89	0.93	Irr	—
230	J044822.79+445528.2	72.095	44.925	160.406	−0.018	0.17	46.87	3.19	17.10 ± 0.04	16.22 ± 0.03	15.72 ± 0.05	0.84	1.02	Irr	—
231	J045144.68+455508.4	72.936	45.919	160.020	1.072	0.63	0.58	4.87	17.34 ± 0.04	16.23 ± 0.03	15.74 ± 0.05	1.16	1.09	ℓS	—
232	J044706.85+453448.3	71.779	45.580	159.761	0.235	0.39	36.30	3.36	17.28 ± 0.04	16.31 ± 0.03	15.75 ± 0.04	1.25	0.99	ℓS	4994
233	J044926.38+445450.8	72.360	44.914	160.534	0.119	0.57	59.34	4.18	17.10 ± 0.03	16.21 ± 0.03	15.75 ± 0.04	0.92	0.96	eS	—
234	J044930.28+443329.0	72.376	44.558	160.815	−0.101	0.51	−64.84	3.81	16.99 ± 0.03	16.12 ± 0.03	15.79 ± 0.05	0.76	0.87	ℓS	—
235	J045109.62+450323.9	72.790	45.057	160.620	0.444	0.47	−35.74	3.64	17.15 ± 0.03	16.20 ± 0.03	15.79 ± 0.04	0.93	0.96	ℓS	—
236	J045517.43+450155.5	73.823	45.032	161.100	0.993	0.28	47.83	3.35	17.13 ± 0.03	16.17 ± 0.03	15.79 ± 0.04	0.90	0.96	Irr	—
237	J045401.45+451107.1	73.506	45.185	160.841	0.916	0.03	−22.56	2.69	17.14 ± 0.03	16.20 ± 0.03	15.80 ± 0.04	0.96	0.93	Irr	—
238	J044452.40+443535.1	71.218	44.593	160.255	−0.707	0.13	−44.30	2.75	17.23 ± 0.04	16.27 ± 0.03	15.83 ± 0.05	1.01	0.97	Irr	—
239	J044936.24+450910.5	72.401	45.153	160.370	0.294	0.16	−26.71	2.74	17.24 ± 0.04	16.27 ± 0.03	15.84 ± 0.04	0.97	0.97	Irr	—
240	J044727.80+444723.1	71.866	44.790	160.400	−0.230	0.68	−44.49	6.25	17.08 ± 0.04	16.32 ± 0.04	15.87 ± 0.07	0.88	0.83	Irr	7288
241	J044428.93+443630.5	71.121	44.608	160.197	−0.750	0.07	41.10	2.86	17.40 ± 0.04	16.46 ± 0.04	15.97 ± 0.06	1.06	0.96	Irr	—
242	J044746.91+453420.6	71.945	45.572	159.843	0.319	0.30	−41.46	3.09	17.48 ± 0.04	16.45 ± 0.03	15.99 ± 0.05	1.23	0.96	Irr	—

Table B – Continued

ID no.	Unique ID	RA	Dec	ℓ	b	ϵ_K	ϕ_K	r_{K20}	J_{K20}	H_{K20}	K_{K20}	$E(B\text{-}V)$	J^o-K^o	Type	v_{rad}
	ZoA	deg	deg	deg	deg		deg	$''$	mag	mag	mag	mag	mag		km s^{-1}
(1)	(2)	(3)	(4)	(5)	(6)	(7)	(8)	(9)	(10)	(11)	(12)	(13)	(14)	(15)	(16)
243	J045143.79+444623.9	72.932	44.773	160.902	0.341	0.45	43.24	3.42	17.32 ± 0.04	16.37 ± 0.03	16.02 ± 0.06	0.88	0.91	Irr	—
244	J044846.14+455955.0	72.192	45.999	159.628	0.725	0.34	29.77	3.04	17.61 ± 0.05	16.60 ± 0.04	16.10 ± 0.05	1.18	1.01	ℓS	—
245	J044942.24+452830.7	72.426	45.475	160.134	0.514	0.07	−32.30	2.56	17.45 ± 0.04	16.49 ± 0.03	16.10 ± 0.05	1.04	0.90	Irr	—
246	J045533.75+445954.9	73.891	44.999	161.157	1.009	0.20	−60.40	2.72	17.44 ± 0.04	16.50 ± 0.03	16.10 ± 0.05	0.91	0.94	Irr	—
247	J045024.44+453101.5	72.602	45.517	160.181	0.636	0.11	−61.08	2.70	17.78 ± 0.05	16.77 ± 0.04	16.28 ± 0.07	1.16	1.00	Irr	—
248	J044758.33+440708.0	71.993	44.119	160.975	−0.593	0.53	−81.40	3.07	17.66 ± 0.04	16.84 ± 0.04	16.38 ± 0.06	0.64	1.00	ℓS	—
249	J044644.16+442005.1	71.684	44.335	160.667	−0.623	0.56	−74.98	3.12	17.66 ± 0.04	16.81 ± 0.04	16.47 ± 0.07	0.73	0.88	mS	5654
250	J044602.99+445836.4	71.512	44.977	160.099	−0.299	0.33	−63.40	3.07	17.87 ± 0.05	17.24 ± 0.05	16.47 ± 0.07	0.96	0.99	Irr	—
251	J045222.42+450342.7	73.093	45.062	160.752	0.612	0.33	−74.00	2.64	18.03 ± 0.05	17.02 ± 0.04	16.57 ± 0.07	0.91	1.07	Irr	—
252	J045430.84+444644.9	73.628	44.779	161.211	0.727	0.68	5.66	2.85	18.45 ± 0.06	17.50 ± 0.05	17.08 ± 0.09	0.88	0.99	ℓS	—
253	J045302.36+454133.4	73.260	45.693	160.338	1.102	0.74	−73.61	3.78	18.56 ± 0.06	17.68 ± 0.05	17.09 ± 0.08	1.11	1.00	Irr	—
254	J044817.36+445352.2	72.072	44.898	160.416	−0.048	0.95	−33.50	11.71	18.42 ± 0.09	17.67 ± 0.09	17.17 ± 0.15	0.84	0.89	Irr	—
255	J045034.26+435930.6	72.643	43.992	161.370	−0.320	0.60	−48.07	2.10	19.24 ± 0.10	18.93 ± 0.13	17.81 ± 0.13	0.64	1.16	Irr	5724
256	J044602.10+443424.5	71.509	44.573	160.400	−0.560	0.05	68.79	1.51	19.00 ± 0.11	18.07 ± 0.09	17.85 ± 0.19	0.94	0.74	Irr	6281
257	J045426.93+444941.5	73.612	44.828	161.170	0.750	0.24	69.67	1.38	19.29 ± 0.09	18.44 ± 0.08	18.05 ± 0.15	0.89	0.85	Irr	5072
258	J045217.47+450839.9	73.073	45.144	160.680	0.650	0.56	43.93	1.78	19.72 ± 0.11	18.84 ± 0.09	18.27 ± 0.15	0.87	1.07	Irr	6680
259	J044644.76+444734.7	71.687	44.793	160.320	−0.320	0.19	75.89	0.94	19.83 ± 0.12	18.84 ± 0.09	18.80 ± 0.24	0.89	0.65	Irr	5709
260	J044838.16+454506.4	72.159	45.752	159.800	0.550	0.35	−77.10	1.07	21.83 ± 0.74	19.89 ± 0.27	18.96 ± 0.24	1.14	2.37	Irr	5745
261	J045026.76+451130.7	72.612	45.192	160.440	0.430	0.63	−53.75	0.73	21.77 ± 0.35	20.25 ± 0.17	20.07 ± 0.39	1.02	1.26	Irr	4639

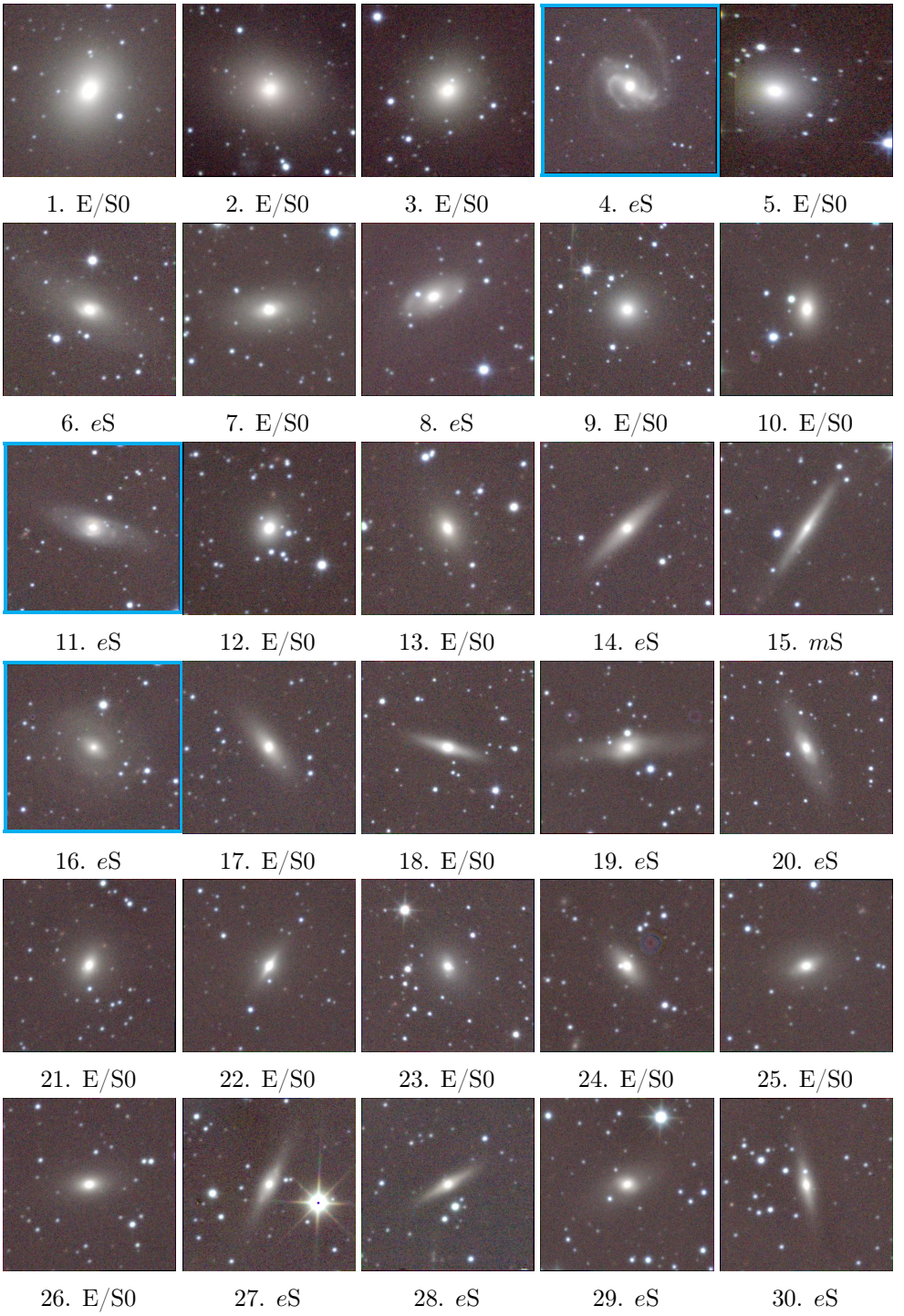

Figure B. The false-colour − J (blue), H (green) and K (red) representation ($1.2'$ × $1.2'$) of the 3C 129 cluster galaxies. The cyan frames indicate HI detection in the WSRT HI-survey.

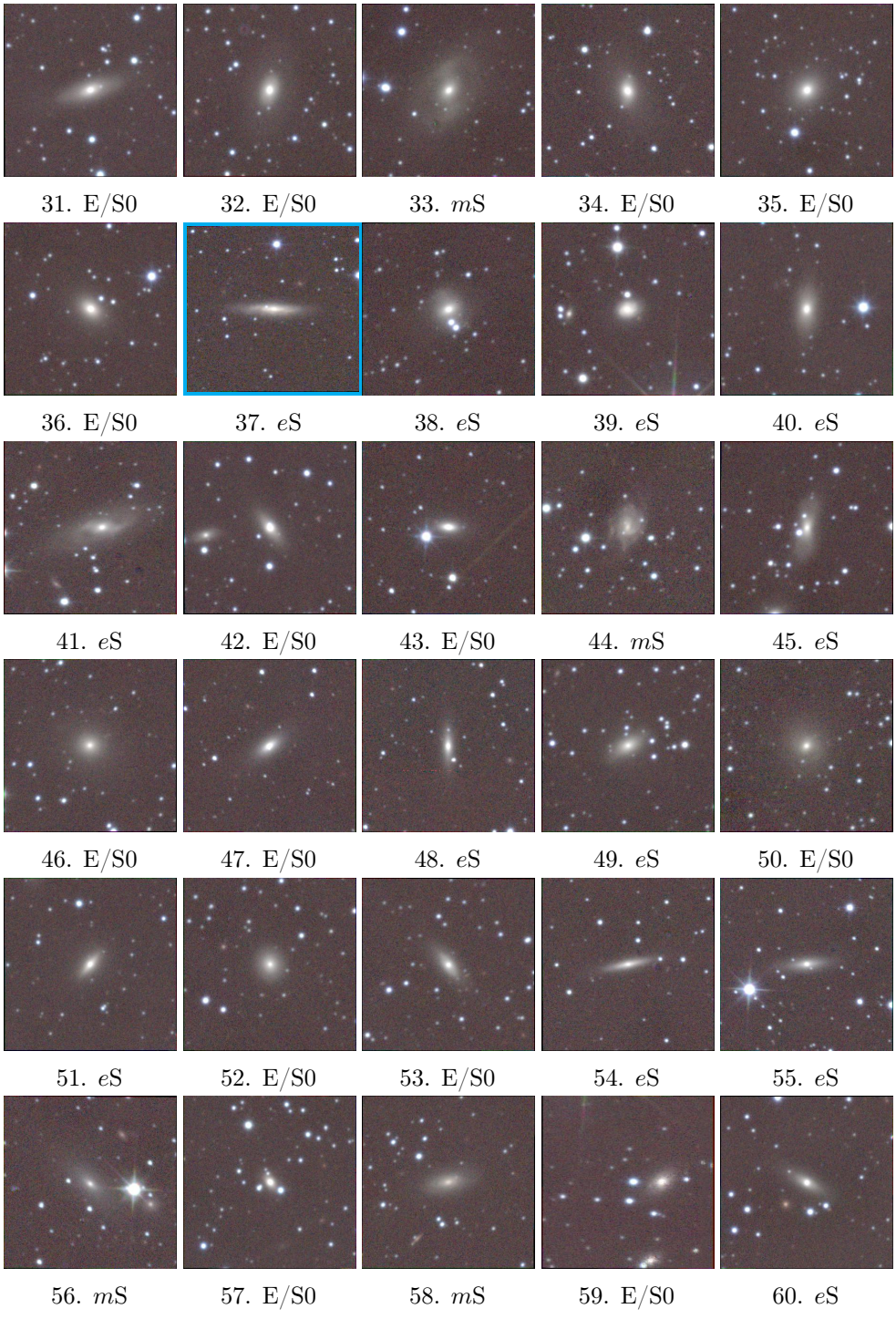

Figure B – Continued.

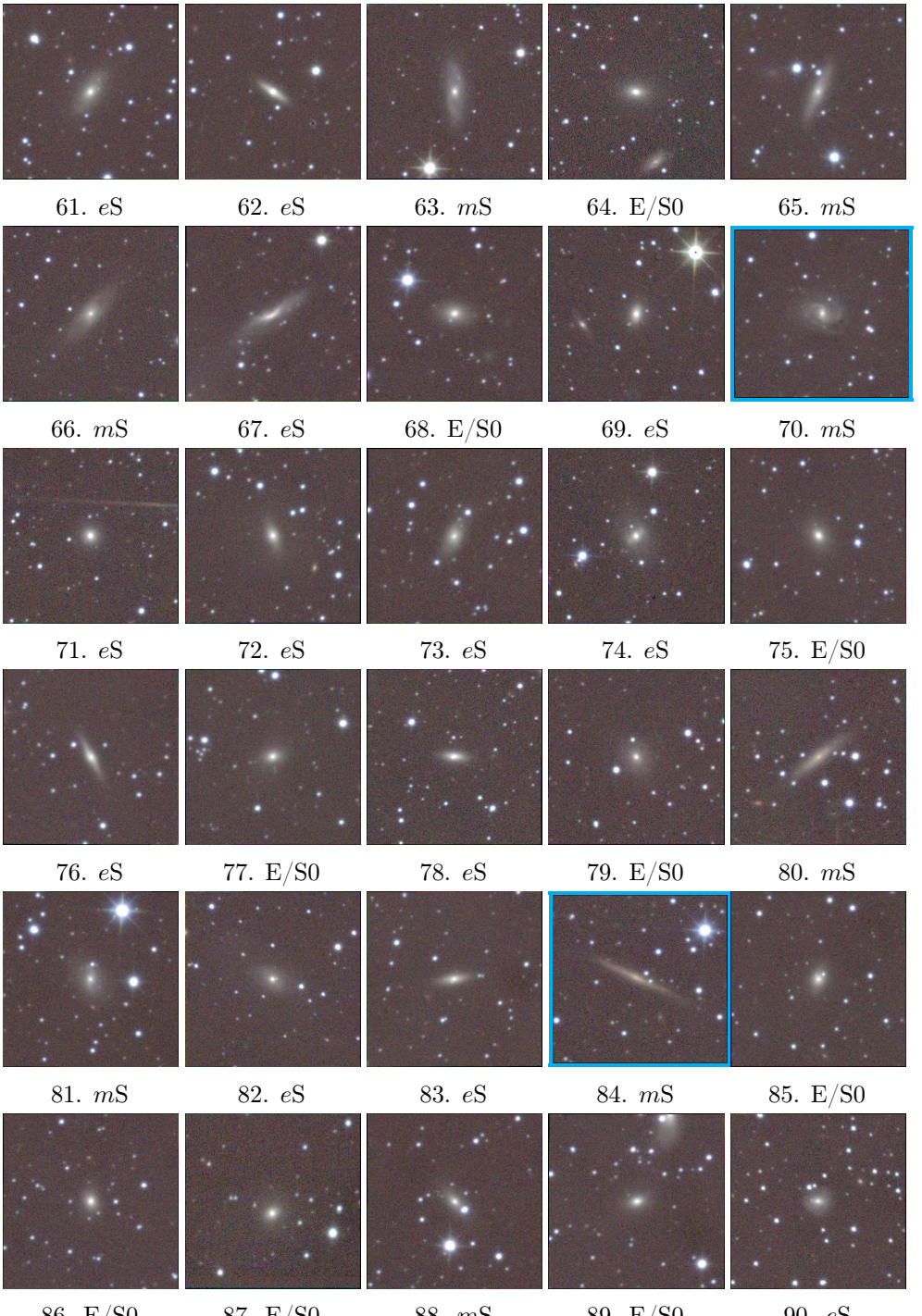

Figure B – Continued.

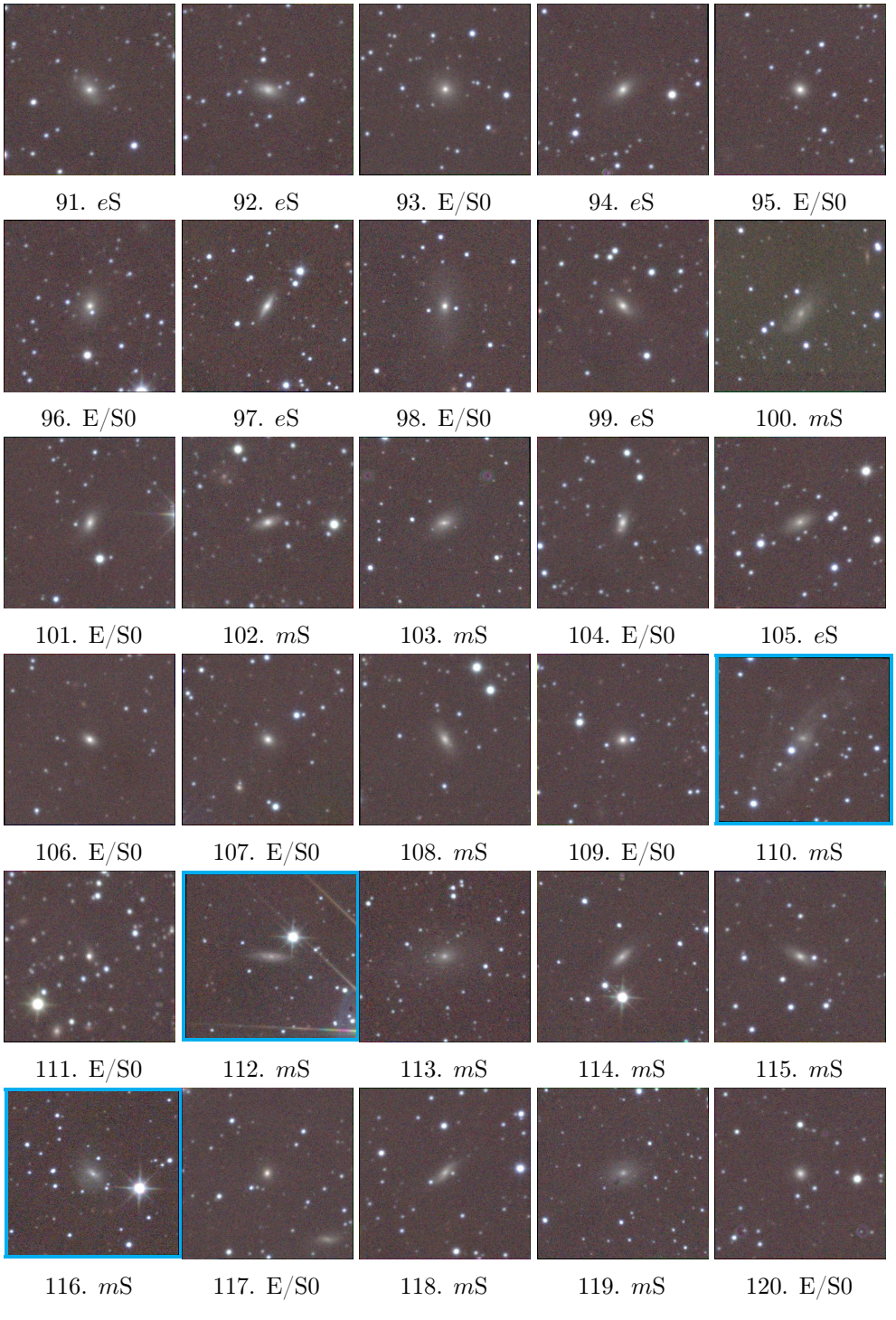

Figure B – Continued.

121. E/S0 122. E/S0 123. mS 124. E/S0 125. E/S0

126. mS 127. mS 128. mS 129. E/S0 130. E/S0

131. mS 132. eS 133. mS 134. eS 135. eS

136. E/S0 137. mS 138. mS 139. mS 140. Irr

141. E/S0 142. mS 143. eS 144. mS 145. mS

146. eS 147. mS 148. ℓS 149. E/S0 150. E/S0

Figure B – Continued.

151. E/S0 152. E/S0 153. ℓS 154. ℓS 155. mS

156. eS 157. mS 158. E/S0 159. mS 160. ℓS

161. mS 162. E/S0 163. eS 164. mS 165. mS

166. mS 167. mS 168. eS 169. Irr 170. mS

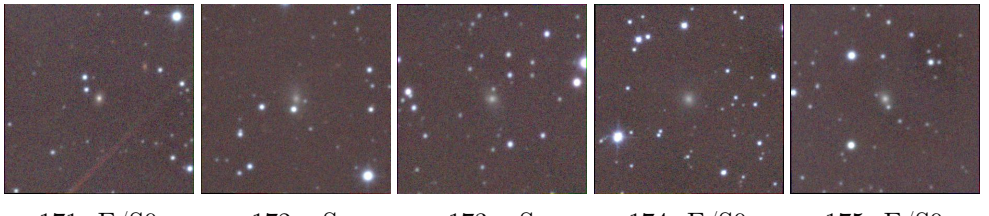

171. E/S0 172. eS 173. eS 174. E/S0 175. E/S0

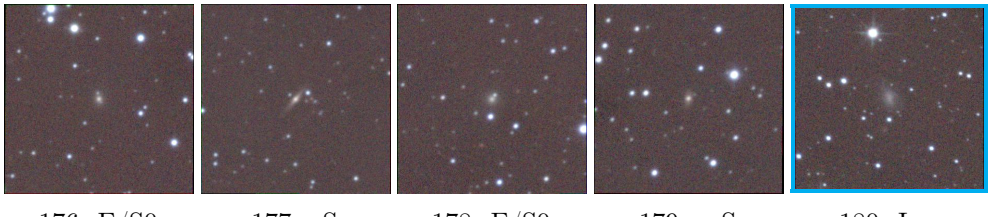

176. E/S0 177. eS 178. E/S0 179. mS 180. Irr

Figure B – Continued.

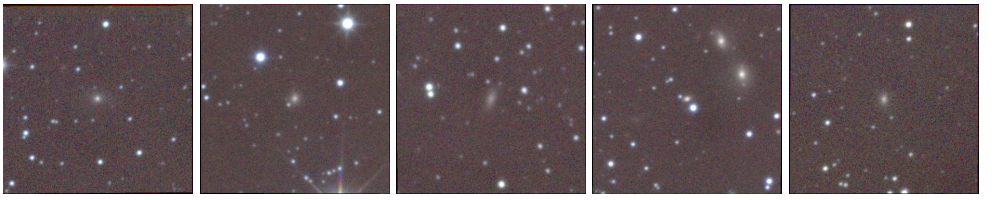

181. E/S0 182. mS 183. ℓS 184. E/S0 185. Irr

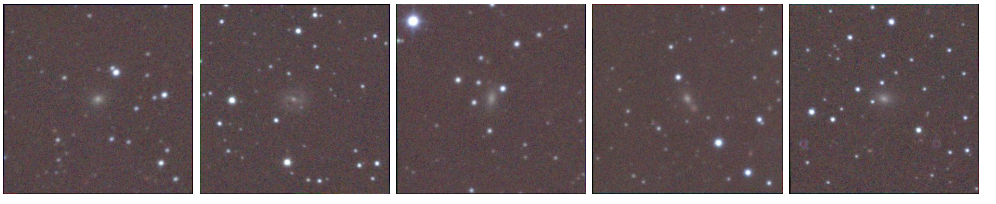

186. ℓS 187. mS 188. ℓS 189. Irr 190. ℓS

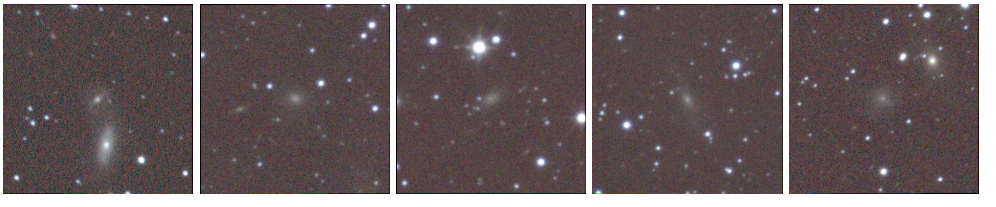

191. mS 192. ℓS 193. ℓS 194. eS 195. mS

196. ℓS 197. ℓS 198. ℓS 199. eS 200. ℓS

201. ℓS 202. ℓS 203. ℓS 204. Irr 205. Irr

206. mS 207. Irr 208. mS 209. ℓS 210. Irr

Figure B – Continued.

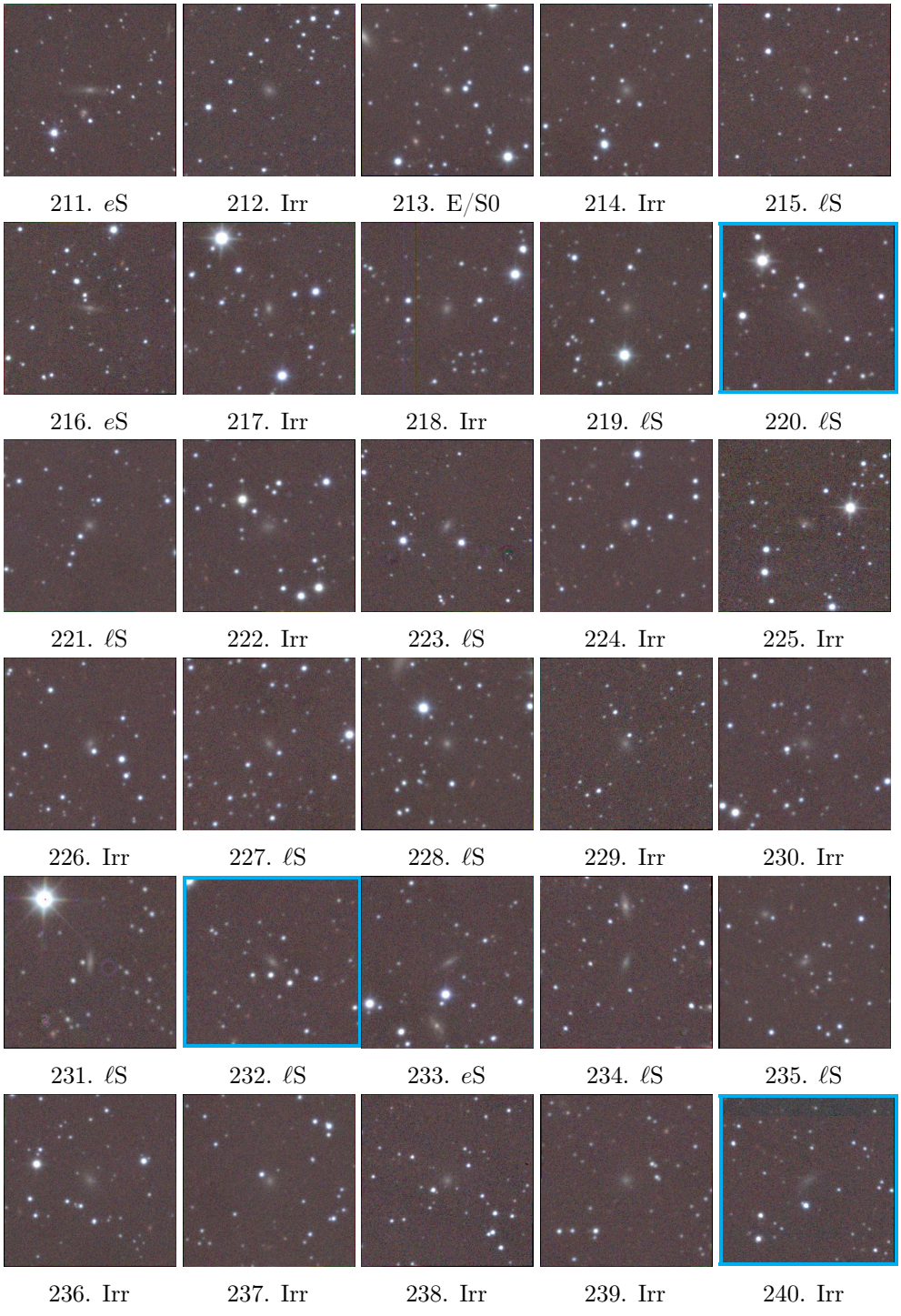

Figure B – Continued.

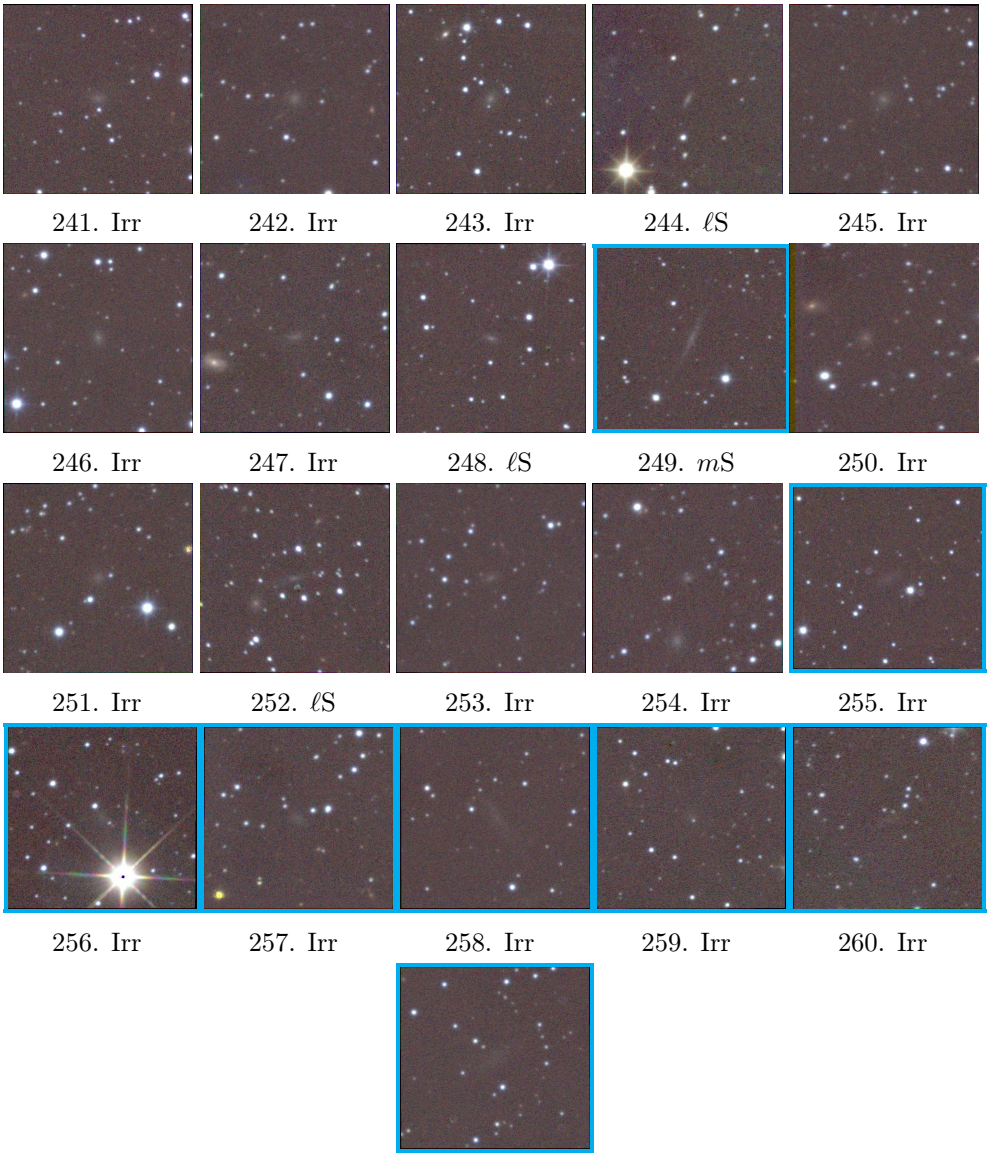

241. Irr 242. Irr 243. Irr 244. ℓS 245. Irr

246. Irr 247. Irr 248. ℓS 249. mS 250. Irr

251. Irr 252. ℓS 253. Irr 254. Irr 255. Irr

256. Irr 257. Irr 258. Irr 259. Irr 260. Irr

261. Irr

Figure B – Continued.